Molecular Cell

Article

Autophagy preferentially degrades non-fibrillar polyQ aggregates

Graphical abstract

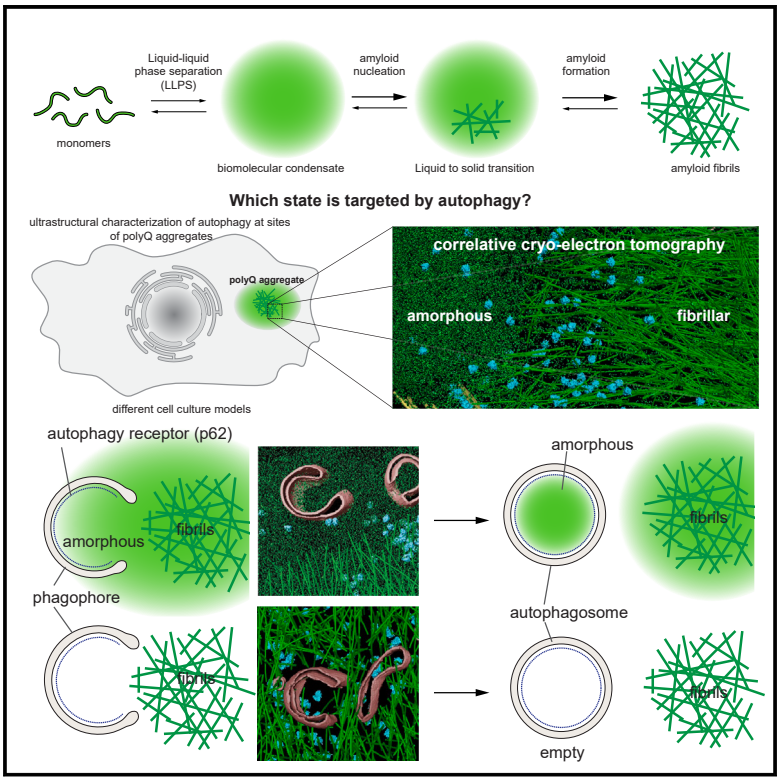

Highlights

- Correlated cryo-ET reveals fibrillar and amorphous state of polyQ aggregates *in situ*
- Autophagy preferentially engulfs amorphous polyQ mediated by the autophagy receptor p62
- Fibrillar polyQ excludes p62 and evades autophagosome engulfment
- Solid polyQ aggregates can trap and arrest the autophagy machineries

Authors

Dorothy Y. Zhao, Felix J.B. Bäuerlein, Itika Saha, F. Ulrich Hartl, Wolfgang Baumeister, Florian Wilfling

Correspondence

dzhao@biochem.mpg.de (D.Y.Z.), uhartl@biochem.mpg.de (F.U.H.), baumeist@biochem.mpg.de (W.B.), florian.wilfling@biophys.mpg.de (F.W.)

In brief

Zhao et al. investigated the interactions between polyQ aggregates and the autophagy machinery in a native cellular environment using correlative cryo-electron tomography. While the fibrillar amyloids showed a lack of autophagy intake, the amorphous polyQ phase is preferentially engulfed upon productive interactions with the autophagy receptor p62.

Zhao et al., 2024, Molecular Cell *84*, 1980–1994
May 16, 2024
https://doi.org/10.1016/j.molcel.2024.04.018

CellPress

CellPress
OPEN ACCESS

Molecular Cell

Article

Autophagy preferentially degrades non-fibrillar polyQ aggregates

Dorothy Y. Zhao,[1,2,6,7,*] Felix J.B. Bäuerlein,[2,3,4] Itika Saha,[5,7] F. Ulrich Hartl,[5,7,*] Wolfgang Baumeister,[2,7,*] and Florian Wilfling[1,2,6,7,8,*]

[1]Max Planck Institute of Biochemistry, Molecular Machines and Signaling, 82152 Martinsried, Germany
[2]Max Planck Institute of Biochemistry, Molecular Structural Biology, 82152 Martinsried, Germany
[3]University Medical Center Göttingen, Institute of Neuropathology, 37077 Göttingen, Germany
[4]Cluster of Excellence "Multiscale Bioimaging: from Molecular Machines to Networks of Excitable Cells" (MBExC), University of Göttingen, 37077 Göttingen, Germany
[5]Max Planck Institute of Biochemistry, Cellular Biochemistry, 82152 Martinsried, Germany
[6]Max Planck Institute of Biophysics, Mechanisms of Cellular Quality Control, 60438 Frankfurt, Germany
[7]Aligning Science Across Parkinson's (ASAP) Collaborative Research Network, Chevy Chase, MD 20815, USA
[8]Lead contact
*Correspondence: dzhao@biochem.mpg.de (D.Y.Z.), uhartl@biochem.mpg.de (F.U.H.), baumeist@biochem.mpg.de (W.B.), florian.wilfling@biophys.mpg.de (F.W.)
https://doi.org/10.1016/j.molcel.2024.04.018

SUMMARY

Aggregation of proteins containing expanded polyglutamine (polyQ) repeats is the cytopathologic hallmark of a group of dominantly inherited neurodegenerative diseases, including Huntington's disease (HD). Huntingtin (Htt), the disease protein of HD, forms amyloid-like fibrils by liquid-to-solid phase transition. Macroautophagy has been proposed to clear polyQ aggregates, but the efficiency of aggrephagy is limited. Here, we used cryo-electron tomography to visualize the interactions of autophagosomes with polyQ aggregates in cultured cells *in situ*. We found that an amorphous aggregate phase exists next to the radially organized polyQ fibrils. Autophagosomes preferentially engulfed this amorphous material, mediated by interactions between the autophagy receptor p62/SQSTM1 and the non-fibrillar aggregate surface. In contrast, amyloid fibrils excluded p62 and evaded clearance, resulting in trapping of autophagic structures. These results suggest that the limited efficiency of autophagy in clearing polyQ aggregates is due to the inability of autophagosomes to interact productively with the non-deformable, fibrillar disease aggregates.

INTRODUCTION

Numerous neurodegenerative disorders (NDs), including Alzheimer's disease, Parkinson's disease, amyotrophic lateral sclerosis, and Huntington's disease (HD), are associated with the formation of toxic aggregates in neuronal cells.[1–3] HD, characterized by a progressive motor and cognitive decline, is the most frequent member of a group of NDs caused by dominantly inherited polyglutamine (polyQ) repeat expansions in otherwise unrelated proteins.[4–6] Expansion of the polyQ sequence in exon 1 of the protein huntingtin (Htt) beyond ~37Q is a strong predictor of HD.[4,5,7,8] The length of the polyQ tract correlates positively with aggregation propensity and disease severity and inversely with the age of disease onset.[4,5] Longer repeats (up to >100 Q) more readily form amyloid-like fibrils, giving rise to highly stable nuclear and cytosolic inclusion bodies,[9,10] initially in striatal neurons, followed by other brain regions as pathology progresses.[4,5,9]

Aggregates of polyQ-expanded Htt display structurally different forms, including dynamic soluble oligomers and stable fibrils with cross-β structure.[10–18] Recently, an amorphous gel-like state has been described as an intermediate stage of fibril formation in yeast and mammalian cells.[19] While the soluble oligomers are recognized as major toxic agents due to their ability to aberrantly engage various cellular machineries,[16,17,20–23] the inclusions, though apparently less toxic,[24–26] contribute to cytopathology by sequestering key cellular proteins and physically disrupting sub-cellular membrane structures.[12,14,16,22,27]

Mammalian cells, including neurons, employ two major pathways for the clearance of misfolded and aggregated proteins, the ubiquitin-proteasome system (UPS) and macroautophagy (hereafter autophagy). Stable aggregates are not directly accessible to the UPS for steric reasons.[28–32] Their clearance requires either chaperone-mediated disaggregation prior to proteolysis[33–35] or encapsulation by autophagosomes for lysosomal degradation.[36–41] The significance of the autophagy pathway is underscored by the finding that mutations in its core components are associated with neurodegenerative diseases, including mutations in p62/sequestosome (SQSTM1) and

optineurin (OPTN), and possibly ubiquilin 2 (UBQLN2), which is more closely linked to the UPS pathway.[42–46] Indeed, autophagy has been implicated in aggregate clearance in a range of neurodegenerative diseases,[44,45,47–49] prominently including HD and other polyQ expansion disorders.[41,50,51] Autophagy of Htt inclusions involves recognition of ubiquitylated Htt[9,52] by the autophagy adaptor protein p62, which forms a bridge between cargo and the protein MAP1LC3B (LC3B) anchored to the autophagosome membrane[42,53] and condenses the cargo through oligomerization.[54] Downstream of the pathway, cargo-containing autophagosomes fuse with lysosomes for content degradation. Based on results from model systems, activation of autophagy by stimulating 5′ AMP-activated protein kinase (AMPK) with agents such as trehalose or inhibition of mTOR with rapamycin or torin1 can ameliorate aggregate cytopathology in a number of model systems.[51,55–58]

Exactly how aggregates are recognized and engulfed by autophagy has remained elusive. The process appears to be of limited efficiency, and it has been suggested that polyQ aggregates are typically too large to be engulfed.[12] In this study, we employed cryo-correlative light and electron microscopy (cryo-CLEM) to visualize the engagement of Htt polyQ aggregates by autophagosomes *in situ*. We find that autophagy preferentially targets the amorphous polyQ phase, which interacts productively with p62. In contrast, the amyloid-like fibrils exclude p62 and evade phagophore engulfment. Solidification of the amorphous polyQ phase tends to trap the autophagic machinery. These results can explain the limited efficiency of autophagy in clearing solid polyQ aggregates.

RESULTS

PolyQ aggregates varying in repeat length are differentially targeted by autophagy

To test the role of autophagy in the clearance of polyQ aggregates in neuronal cells, we expressed ecdysone-regulated Htt exon 1-GFP fusion proteins with repeats of 64Q and 150Q.[16,59] After 48 h of induction with muristerone A, protein aggregates of different sizes were visible by confocal fluorescence light microscopy (Figure S1A). Most 64Q appeared to be diffuse in the cell, with ~10% of cells harboring small aggregates of varying brightness. In contrast, 150Q formed large GFP-intense globular structures that were previously observed to contain amyloid-like fibrils.[12] To monitor aggrephagy, we co-expressed as a marker the mammalian Atg8 homolog MAP1LC3B/LC3B, which is conjugated to phosphatidylethanolamine of the phagophore membrane during phagophore biogenesis. mCherry-LC3B co-localized with 64Q but not with the aggregates of 150Q (Figure 1A). Similarly, Lamp1-RFP, a lysosomal marker, also co-localized with 64Q but not with the 150Q aggregates (Figure 1B), suggesting a polyQ length-dependent targeting of polyQ aggregates by autophagy.

To compare the autophagic clearance of polyQ aggregates with different polyQ lengths, we monitored the levels of total polyQ-GFP after 6 and 12 h of muristerone A withdrawal by dot blot assay (Figure 1C). Consistent with the differential co-localization of 64Q and 150Q with the autophagic machinery (Figures 1A and 1B), only 64Q, but not the more fibril-prone 150Q, showed a visible reduction by immunoblotting after 12 h of muristerone A withdrawal. To increase autophagic intake, we treated the cells with a combination of trehalose and rapamycin (treh/rapa).[51] Treh/rapa treatment enhanced clearance of 64Q aggregates but not 150Q aggregates (Figure 1C). In contrast, blocking lysosomal degradation with bafilomycin A1 or chloroquine[60] abolished 64Q degradation (Figure 1D), indicating that 64Q is indeed subject to autophagic degradation. Inhibition of the ubiquitin (Ub)-activating enzyme E1 by MLN7243[61] also abolished 64Q degradation (Figure 1D), suggesting that polyQ clearance is a Ub-dependent process.

The Htt polyQ model protein has been shown to undergo a liquid-to-solid phase transition that ultimately drives the aggregation process toward SDS-resistant amyloid fibrils, with the aggregates increasing in fluorescence intensity along this pathway.[19] To gain information about the structural state of the 64Q aggregates, we turned to *in situ* cryo-CLEM (Figures S1B–S1F).[62,63] In short, 64Q-expressing cells were cultured on grids and vitrified by plunge freezing.[64] The GFP signal identified by the cryo-CLEM workflow allowed targeting of the aggregates during lamella preparation using focused ion beam (FIB) milling; tilt-series at correlated regions were subsequently collected by cryo-electron tomography (cryo-ET). In addition to the known fibrillar phase of 64Q,[12] cryo-ET revealed the presence of a structurally amorphous non-fibrillar phase of 64Q. The amorphous 64Q phase corresponded to dim GFP puncta in fluorescence microscopy, much smaller than the large aggregate signal predominantly seen in 150Q (Figure S1A). This amorphous phase contained many double membrane structures, some of which resembled potential phagophores and intermediates in autophagosome formation[65,66] (Figures S1E and S1F). Furthermore, biochemical analysis revealed an ~50% decrease in the total pool of 64Q protein upon treh/rapa enhanced autophagy, although the number of SDS-resistant aggregates was only slightly reduced (Figures 1E–1F), indicating that autophagy preferentially targets non-fibrillar, SDS-soluble Htt aggregates.

It has been suggested that trehalose, besides activation of aggrephagy, may have pleotropic effects, including a chaperone-like function in modulating aggregation and possibly interfering with autophagy flux.[67,68] To rule out such additional effects, we treated the cells only with torin1, a potent specific inhibitor of mTOR. Similar to the treh/rapa treatment, modulation of autophagy by torin1 led to an increased turnover of the total polyQ pool but not of the aggregated fraction (Figures 1G and 1H), confirming that both treatments have similar effects on polyQ clearance by autophagy. Similarly, quantification of fluorescent 64Q aggregates[16] after 12 h of treatments showed a more pronounced effect in the reduction of small 64Q foci (<1 μm) rather than the larger aggregates (>1 μm) with both torin1 and treh/rapa (Figure S1G), in agreement with the literature.[58]

Taken together, these data show that autophagy efficiently removes the SDS-soluble aggregates of 64Q, whereas autophagic clearance is limited for the SDS-resistant, fibrillar aggregates that are predominantly observed with the longer 150Q repeats.

Autophagy affects the different phases of 97Q aggregates

To genetically manipulate polyQ aggrephagy, we expressed 97Q-GFP (97Q) in HEK293 cells, aggregates of which have

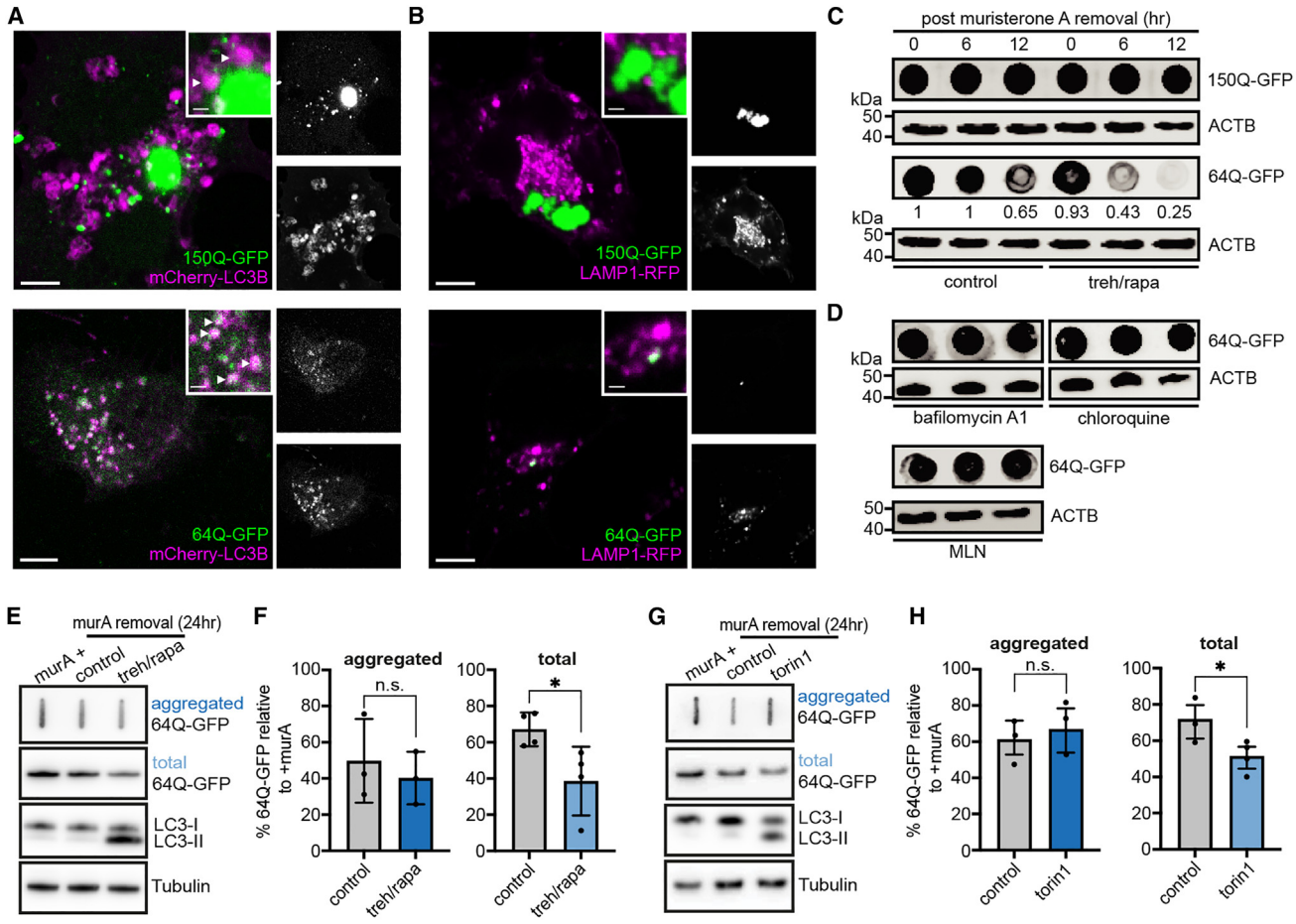

Figure 1. PolyQ aggregates with varying repeats are differentially targeted by autophagy

(A and B) Representative confocal microscopy images of 2-day muristerone A (1 μM)-induced expression of 64Q- and 150Q-GFP in Neuro2a cells, co-expressed with mCherry-LC3B (A) or Lamp1-mCherry (B). Arrowheads indicate polyQ-LC3B interactions. Scale bars: 5 μm and 1 μm (inlay)

(C and D) Dot blots with the indicated antibodies for total 150Q- and 64Q-GFP lysates from cells with 2-day muristerone A induction and removal, with a 1-day concurrent 150 mM treh/200 nM rapa treatment, or with autophagy inhibited by bafilomycin A1 (100 nM) or chloroquine (100 μM), or with Ub-activating enzyme E1 inhibited by MLN7243 (0.2 μM) for 6 or 12 h. ACTB was used as loading control.

(E–H) Slot blot and immunoblot analysis (E, G) with the indicated antibodies for aggregated or total 64Q-GFP with 2-day muristerone A induction and removal, followed by a 1-day 150 mM treh/200 nM rapa (E) or 250 nM torin1 (G) treatment. Tubulin was used as loading control. Quantification with normalization to +muristerone A (100%) (F, H), error bars: SD. $n = 3$ or 4 for immunoblot and slot blot, $^{*}p < 0.05$.

been shown by cryo-ET to form fibrils.[12] As judged by fluorescence light microscopy, 97Q and 150Q aggregates are similar in terms of brightness and prevalence. To monitor the size of the 97Q aggregates during autophagy, we co-labeled cells with either an antibody against LC3B or LysoTracker to stain lysosomes (Figures 2A and 2B). We quantified the cross-sectional areas around the equator of the aggregates as well as signals corresponding to LC3B or LysoTracker within a 1.5 μm distance from the aggregates.[69] To downregulate autophagy, we performed siRNA knockdown of LC3A/B/C[70] or CRISPR-Cas9 knockout of LC3A/B (note that LC3C is below detection in HEK293) and confirmed the reduction of the protein or transcript by immunoblotting and/or real-time PCR, respectively (Figure S2A). Downregulation of LC3A/B by either knockdown or knockout led to a significant accumulation of the aggrephagy receptor p62 as monitored by immunoblotting, suggesting an important role for these proteins in promoting autophagy in HEK293 cells (Figure S2B). Addition of torin1 or treh/rapa (24 h) showed no effect on cell viability as assessed by live Annexin V staining (Figure S2C).

We observed that 97Q aggregates under constitutive expression consisted of two distinct zones: a central zone of high fluorescence intensity and a much dimmer peripheral region surrounding it (Figures 2A, 2B, and S2D). The fluorescence intensity of the peripheral aggregate region under these conditions was only 10%–25% of that of the central zone, indicating a substantially lower 97Q density. Upon LC3 knockdown or knockout, microscopic analysis consistently revealed an increase in the central zone (Figures 2D and S2E), coupled with a loss of LysoTracker signal around the polyQ aggregate (Figure S2I). In addition, the loss of LC3A/B resulted in an enlargement of the peripheral region around the central aggregate

CellPress
OPEN ACCESS

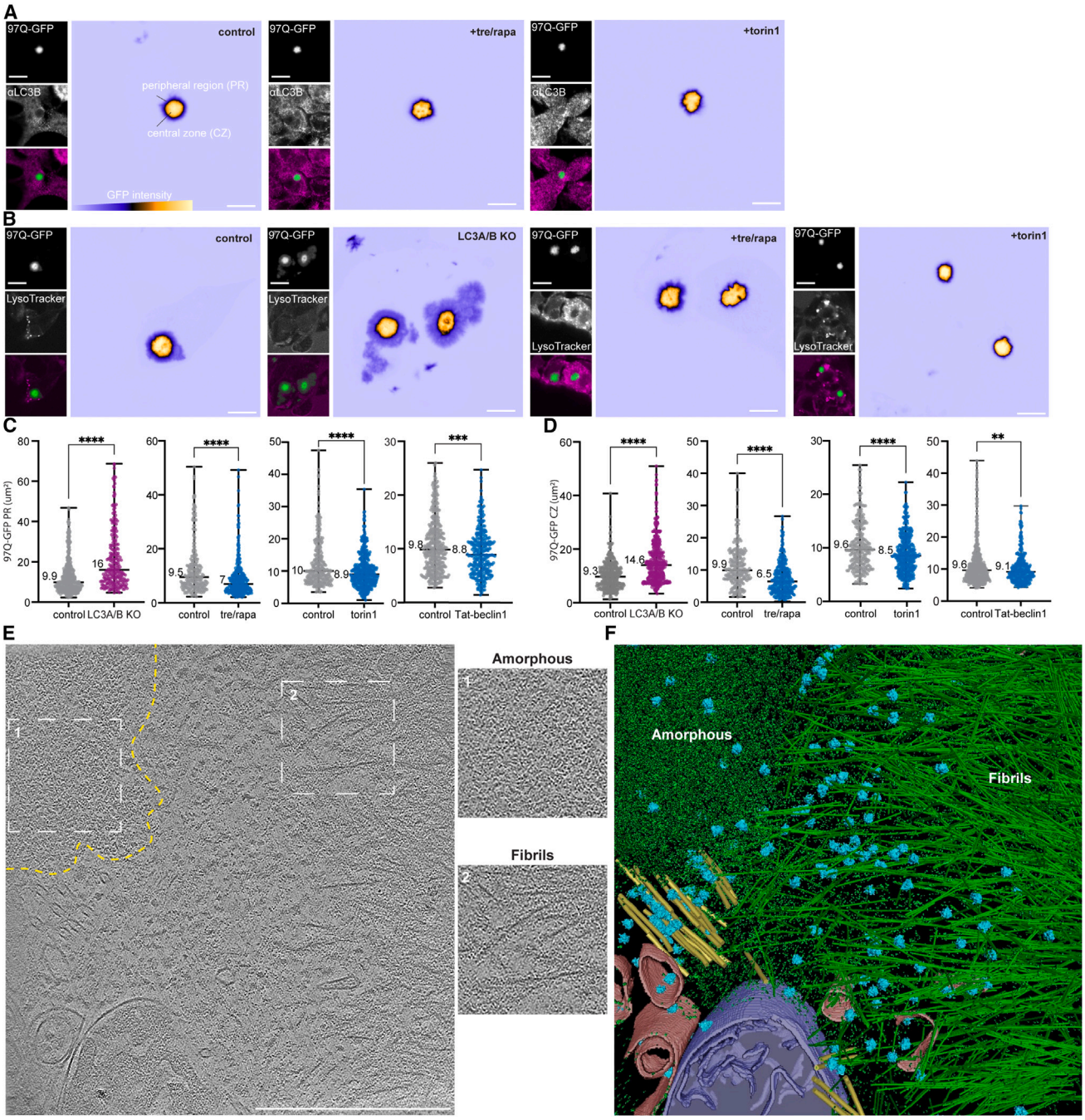

Figure 2. Autophagy affects the different phases of 97Q aggregates

(A and B) Representative confocal images of control, LC3A/B knockout (KO), 1-day 150 mM treh/200 nM rapa, or 200 nM torin1 in HEK293 cells, stained with LC3B antibody (A) or LysoTracker (B).

(C) Image quantification of the 97Q-GFP peripheral aggregate region (PR) in control cells and in LC3A/B knockout cells (control $n = 395$, LC3A/B KO $n = 245$), treh/rapa-treated cells (control $n = 228$, +treh/rapa $n = 310$), torin1-treated cells (control $n = 264$, +torin1 $n = 406$), and cells treated with Tat-beclin1 peptide (control $n = 391$, +30 μM peptide $n = 288$). Median values are displayed, intensity standardized with threshold 800–8,000, $^{****}p < 0.0001$, $^{***}p < 0.001$.

(D) Image quantification of the 97Q-GFP aggregate central zone (CZ) cross-sectional area in control cells and in LC3A/B knockout cells (control $n = 409$, LC3A/B KO $n = 551$), treh/rapa-treated cells (control $n = 226$, +treh/rapa $n = 308$), torin1-treated cells (control $n = 264$, +torin1 $n = 406$), and cells treated with Tat-beclin1 peptide (control $n = 391$, +peptide $n = 288$). Median values are displayed, central zone intensity standardized with threshold >8,000 (Fiji), $^{****}p < 0.0001$, $^{**}p < 0.01$.

(E and F) Tomographic slice of 97Q-GFP at 32,000x (E) and segmentation (F). ER-related membranes (pink), mitochondria (purple), microtubules (yellow), ribosomes (blue), and polyQ (green). Inserts show enlarged amorphous (dotted line) and fibrillar regions. CLEM workflow and lamella view related to (E) and (F) can be found in Figures S3A–S3C.

Scale bars: 5 μm in (A) and (B), 500 nm in (E).

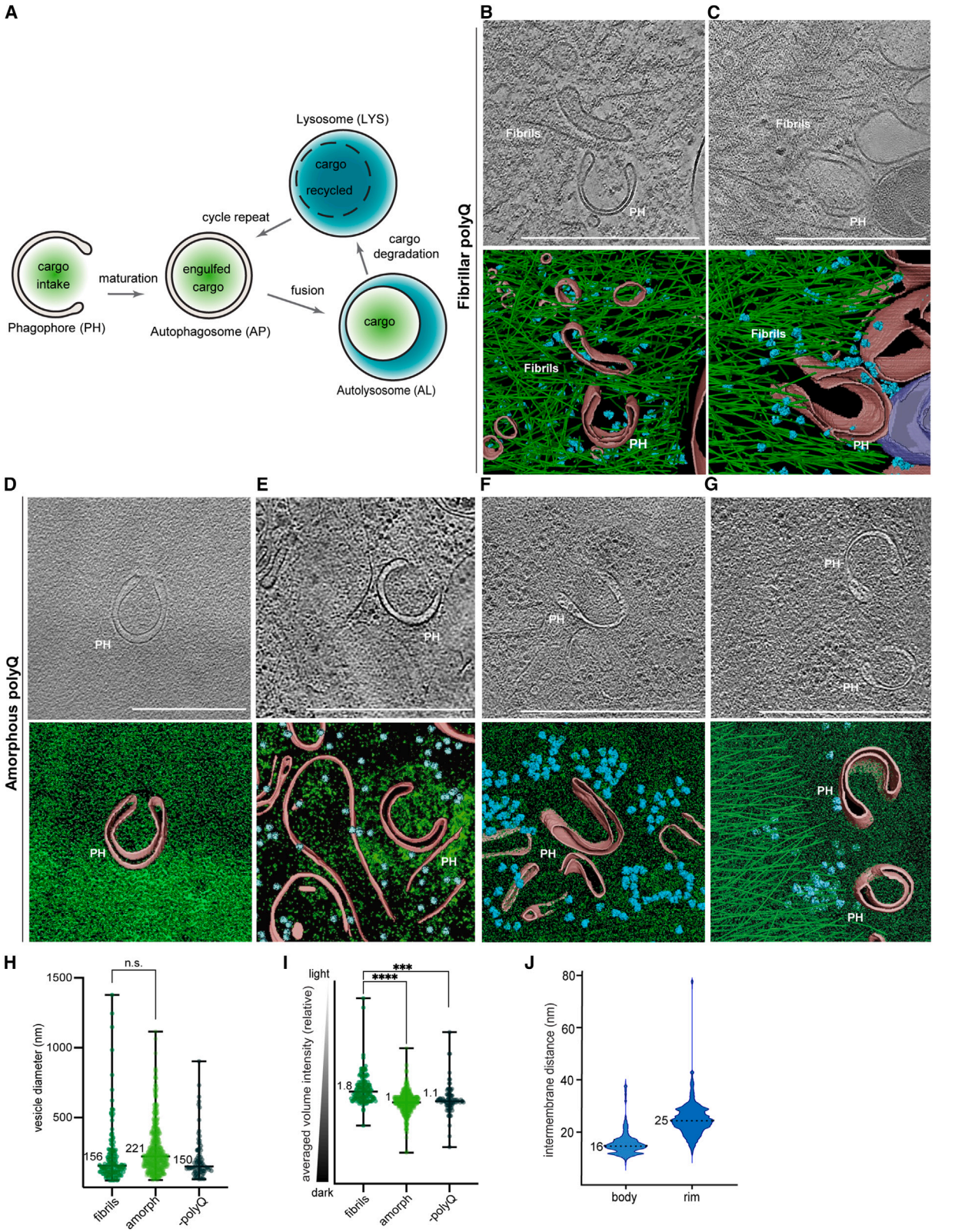

(legend on next page)

zone (Figures 2B, 2C, and S2E). The individual knockdown of LC3A and B or the combinatorial knockdown of GABARAP and GABARAPL2 showed a less pronounced phenotype (Figures S2F and S2G), supporting the functional redundancy among the ATG8 homologs. Pharmacological inhibition of VCP, which is involved in several steps of autophagy activation and is seen enriched around the aggregate (Figure S2H), resulted in some expansion of the central zone. In contrast, enhancement of autophagy by treh/rapa, torin1, or the Tat-beclin1 peptide reduced the size of the aggregates (Figures 2A and 2B), as manifested by a reduction in both the peripheral region and the central zone (Figures 2C and 2D) and an increase in the proximal LysoTracker and LC3B signals (Figures S2I and S2J), suggesting effects of induced autophagy during polyQ aggregate growth. To exclude effects of the GFP-tag on 97Q, we also performed experiments with cells transfected with 97Q-myc, which resulted in similar observations of aggregate expansion upon knockdown of LC3A/B or LC3A/B/C (Figure S2K).

During aggregation, multiple physical states of polyQ Htt are presumably in equilibrium, ranging from liquid-like condensates to solid, amorphous aggregates and end-stage amyloid-like fibrils.[12,14,19] We therefore examined the dynamics of 97Q in the central zone and peripheral region of the aggregates using fluorescence recovery after photo bleaching (FRAP) (Figure S2L). FRAP analysis using a double-normalization method showed that the mobile fraction of 97Q in the central zone was estimated at 0.34 ± 0.08 (mean ± SD) and remained unchanged upon induction of autophagy, indicating that the majority of polyQ in the central zone is immobile regardless of the state of autophagy. In contrast, while the recovery of the peripheral region was similarly low after LC3 knockout (0.32 ± 0.1), the mobile fraction of 97Q increased significantly after autophagy induction with torin1 (0.52 ± 0.2) or treh/rapa (0.68 ± 0.2), or mCherry-LC3B overexpression (0.62 ± 0.3), indicating that autophagy increases the mobile fraction within the peripheral region of the aggregates and counteracts solidification.

To visualize the ultrastructural differences between the central zone and peripheral region of the polyQ aggregate, we again turned to *in situ* cryo-CLEM. Cryo-CLEM analysis of LC3A/B knockout cells expressing 97Q showed that the high GFP intensity of the central zone corresponds to a polyQ fibrillar core, while the lower GFP signal of the peripheral region corresponds to an amorphous polyQ phase, both of which largely excluded ribosomes (Figures 2E, 2F, S2M, and S3A–S3C). In addition, amorphous polyQ appeared in two states: one contained some fibrillar structures within a confined amorphous density consistent with a more solid state and corresponding to a brighter GFP fluorescence (Figures S2M and S3D–S3F); the other state lacked detectable fibrillar structures and corresponded to a weaker GFP signal, which nevertheless separated from the cytosol, as ribosomes were largely excluded from these areas (Figures 2E, 2F, and S2M). Ongoing liquid-to-solid phase transition within the amorphous polyQ phase may explain the low mobility of 97Q in the peripheral region observed by FRAP analysis (Figure S2L).

Aggrephagy preferentially engulfs the amorphous polyQ phase

The results so far suggested that autophagy can only remove an early intermediate in the Htt aggregation pathway (Figures 1 and 2). We next used cryo-CLEM to study the interaction of the autophagy machinery with the aggregates (Figures 3 and S4–S11). A schematic of the expected autophagic structures transitioning from cup-shaped phagophores to bilamellar autophagosomes and fusion of the autophagosome with lysosomes to form autolysosomes for degradation is shown in Figure 3A. To target autophagic structures, cells expressing 97Q with either mCherry-LC3B or HALO-WIPI2B or after LysoTracker staining were used for the cryo-CLEM workflow. To ensure the identity of the structures in the lamella, the thin lamellae were re-imaged in the cryo-confocal microscope after tomogram acquisition to post-correlate the fluorescent signals (Figures S7C, S7K, S9C, and S11C).

The tomograms revealed different autophagic structures close to both fibrillar and amorphous polyQ phases, including phagophores (Figures 3B–3G, S4E, S5–S7, and S9–11), autophagosomes, and autolysosomes with not-yet digested cargo (Figures S4A–S4G and S7–S9). Often these structures appeared to be trapped and isolated in the observed polyQ phases. These trapped structures were morphologically aberrant compared to structures seen previously in cells not expressing polyQ proteins.[66,71] Small phagophores, for example, showed a strong cup-shaped bending, and the intermembrane distance between the inner and outer bilayer of the phagophore membrane was sometimes wider than similar phagophores without polyQ expression (Figure 3J).[66] On average, the intermembrane spacing of the phagophores was found to be 16 ± 5.4 nm for the phagophore body and 25 ± 7.3 nm for the dilated rim area (Figure 3J). These phagophores also lacked contact sites between the phagophore rim and the ER, suggesting that lipid transfer and expansion of the phagophore may be impaired in these cases. Notably, phagophores proximal to or trapped by fibrillar polyQ (Figures 3B and 3C), as well as autolysosomes and lysosomes (Figures S4A–S4D), appeared to contain less cargo material as estimated from the average electron density

Figure 3. Phagophores preferentially interact with amorphous polyQ aggregates *in situ*

(A) Schematic of the different stages of the autophagic degradation pathway.

(B–G) Tomographic slices acquired for 97Q-GFP with LysoTracker staining or mCherry-LC3B or Halo-WIPI2B co-expression upon induced autophagy, for phagophores (PH) proximal to fibrils (B and C) or amorphous polyQ (D–G). Segmentation: PH and ER-related membranes (pink), mitochondria (purple), ribosomes (blue), and polyQ (green).

(H and I) Tomogram quantification: diameter (H) and average interior volume density (I) for phagophores to autophagosomes, proximal to fibrils (n = 143), to amorphous polyQ (n = 584), or in cells without polyQ (n = 81) with median values; ****$p < 0.0001$, ***$p < 0.001$.

(J) Quantification for the intermembrane distances of the phagophore body and rim regions from 22 phagophores. The average distances are 16 ± 5.4 nm and 25 ± 7.3 nm, respectively.

Scale bars: 500 nm in (B)–(G). CLEM and lamella views related to (B) are shown in Figure S5, to (C) are shown in Figure S6, to (D) are shown in Figures S7E–S7H, to (E) are shown in Figures S7I–S7K, to (F) are shown in Figure S10, and to (G) are shown in Figure S11.

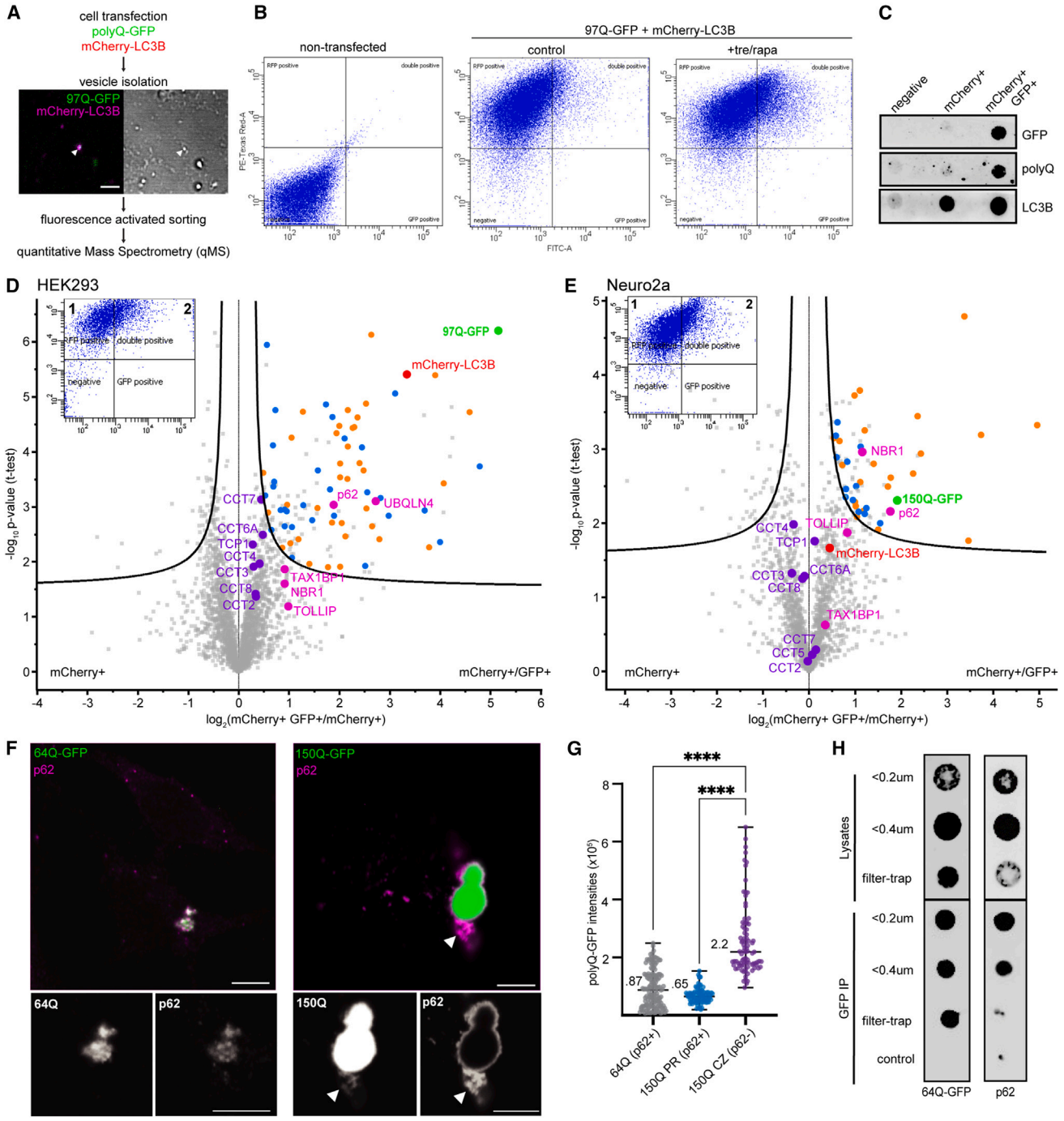

Figure 4. The autophagic intake of the polyQ is a p62-mediated process

(A) Experiment workflow: mCherry-LC3B- and 97Q-GFP-positive vesicles (arrowheads) extracted from co-transfected HEK293, sorted and analyzed by quantitative mass spectrometry.

(B and C) Fluorescence vesicle sorting (~10,000 events) sorted by RFP (y axis) and GFP (x axis); puncta represent individual events (B). Sorted vesicles were validated with the indicated antibodies in dot blots (C).

(D and E) Label-free quantitative mass spectrometry analyses of the sorted vesicles plotted with mCherry+ control versus mCherry+ GFP+. Curves (FDR <0.01) for HEK293 + treh/rapa + chloroquine in (D) and for Neuro2a + treh/rapa + chloroquine in (E). Inserts show vesicle sorting for mass spectrometry with mCherry+ (quadrant 1) and mCherry+ GFP+ (quadrant 2) positive signal. Receptors for Ub-substrates (pink) and TRiC subunits (purple) are highlighted; proteasome and protein quality control regulators (orange) and RNA processing factors (blue) are colored. Chloroquine was included to inhibit degradation of autophagosomal contents for mass spectrometry quantifications.

(F) Representative confocal images of 64Q- and 150Q-GFP stained with antibody against p62. Arrowheads: polyQ-p62 co-localization.

(legend continued on next page)

of the vesicle interior volume, indicating inefficient uptake of fibrillar aggregates. In contrast, phagophores (Figures 3D–3G) and their mature forms (Figures S4E–S4G) located proximal to amorphous polyQ were filled with electron-dense cargo, resembling the surrounding amorphous density. These observations were supported by post-correlation analysis, demonstrating that the lamella regions with the autophagic structures were indeed positive for both 97Q and mCherry-LC3B (Figures S4E–S4G, S7D, and S9D) and Halo-WIPI2B (Figure S11D). To further validate the identity of the observed cup-shaped or bilamellar structures as functioning in autophagy, we tracked the mCherry-LC3B signal in *ULK1*$^{-/-}$ HEK293 cells after torin1 treatment. This analysis confirmed a loss of LC3B-positive vesicle puncta by fluorescence microscopy (Figures S12A and S12B). Instead of observing phagophores or autophagosomes, cryo-CLEM revealed that the mCherry-LC3B-positive cytosol in *ULK1*$^{-/-}$ cells showed an expansion of the endo-lysosomal system, as indicated by the accumulation of small vesicular structures (Figures S12C–S12E). Consistent with the loss of autophagic structures, the size of the 97Q-GFP aggregate central zone and peripheral region expanded upon ULK1 knockout, coupled with a decrease in the LysoTracker signal proximal to the aggregate (Figures S12F–S12G), similar to the loss of LC3A/B.

Strikingly, phagophores also appeared to be "trapped" in a dense amorphous polyQ phase devoid of other cellular components, suggesting that a potential solidification of the polyQ phase may block phagophore maturation (Figure 3D). To further test this possibility, we co-transfected cells with 97Q-myc and the autophagic flux reporter GFP-LC3B-RFP.[72] The GFP-LC3-RFP reporter is cleaved in the linker between LC3 and RFP by the activating enzyme Atg4, resulting in equimolar amounts of GFP-LC3 and RFP. While GFP-LC3 is lipidated and subsequently degraded during autophagy, RFP serves as an internal expression control, allowing the determination of autophagic flux based on the GFP/RFP signal ratio. Strikingly, this analysis revealed that the reporter signals around the large aggregate core were green-shifted (Figure S4H) and completely immobile for an extended period of time during time-lapse microscopy (Figure S4I), indicating a block of autophagic turnover. Several sites of ER-phagy were also observed proximal to the aggregates (Figures S4E and S4G), containing ER cargo but again lacking fibrillar polyQ content.

Using ~300 tomograms, we categorized vesicular membrane structures of the autophagic pathway (corresponding to phagophores, autophagosomes, autolysosomes, and lysosomes) (Figures 3H, 3I, S4J, and S4K) as proximal either to fibrils or to amorphous polyQ. Cells without polyQ overexpression were included as control in this survey. These vesicular membrane structures were then analyzed for their dimensions and cargo density. No significant size difference was observed for vesicular membrane structures in the three categories, as they covered a wide range of vesicle diameters (Figure 3H). However, the average density within the volume of the inner vesicular membrane structures proximal to fibrils was significantly lower than the density of the entire tomogram (Figure 3I), suggesting depletion of cargo. The downstream vesicles in the vicinity of fibrils also showed a similar depletion of cargo within the membrane-enclosed space, as measured by the average intensity of the interior volume (Figure S4K); they were smaller than those proximal to amorphous polyQ, possibly due to fibril-induced deformation (Figure S4J). In conclusion, *in situ* cryo-CLEM indicates that autophagic structures preferentially interact with and engulf the amorphous phase of polyQ aggregates and not the fibrillar form.

Autophagic targeting of polyQ is a p62-mediated process

Recently, the CCT2 subunit of the chaperonin TRiC/CCT was reported to serve as a Ub-independent selective autophagy receptor for the removal of solid polyQ aggregates.[73] To identify the autophagy receptor for polyQ in an unbiased manner, we established a protocol to isolate polyQ-containing autophagosomes and analyze their contents by label-free quantitative mass spectrometry.[74] Vesicles were isolated from cells co-expressing 97Q and mCherry-LC3B and subjected to fluorescence sorting[75] (Figure 4A). Fluorescence sorting revealed that 10% of the total mCherry-LC3B vesicle pool in double-transfected cells were positive for both mCherry-LC3B and 97Q, indicating that the cells have a modest basal autophagic activity for polyQ. Treatment of cells with treh/rapa, but not torin1, increased this percentage to 25%, allowing enhanced trapping of 97Q in the autophagosomes (Figure 4B).

Next, the sorted non-fluorescent (negative), mCherry-positive (mCherry+), and mCherry/GFP double-positive vesicles (mCherry+/GFP+) were examined in dot blot experiments to confirm the presence of LC3B and polyQ by immunoblotting (Figure 4C). The sorted vesicles from HEK293 and Neuro2a cells were then analyzed by mass spectrometry (Figures 4D, 4E, and S13A–S13C). The mCherry+/GFP+ vesicles from both cell systems were strongly enriched for polyQ-GFP in comparison to the mCherry+ control vesicles (Figures 4D, 4E, S13A, and S13B). From both cell types, quantitative mass spectrometry revealed a significant enrichment of the Ub-dependent autophagy receptor p62 with polyQ, especially upon chloroquine (Figures 4D and 4E) or bafilomycin A1 (Figure S13B) treatment (FDR <0.01). Numerous proteasome subunits, regulators of protein quality control, and proteins with low complexity sequences (e.g., FUS, TARDBP), previously found to interact with polyQ,[16,76] were also enriched (Figures 4D, 4E, S13A, and S13B). However, there was no enrichment of the proposed aggrephagy receptor CCT2[73] compared to subunits of the TRiC complex or the entire quantified autophagosome proteome.

Next, we validated the roles of Ub and p62 in polyQ autophagy (Figures 4F–4H and S13D–S13K). The requirement for ubiquitylation in polyQ degradation was confirmed using treatment with the E1 inhibitor MLN7243 (Figure 1D), which resulted in a

(G) Image quantification of 64Q-GFP (n = 148) and 150Q-GFP (n = 87) for GFP intensities with p62 co-localization, with median values displayed. CZ, aggregate central zone; PR, peripheral region. ****p < 0.0001.
(H) 64Q-GFP lysate filter partitioned followed by anti-GFP pull down, for the detection with the indicated antibodies in each fraction in dot blots (n = 3).
Scale bars: 2 μm in (A), 5 μm in (F).

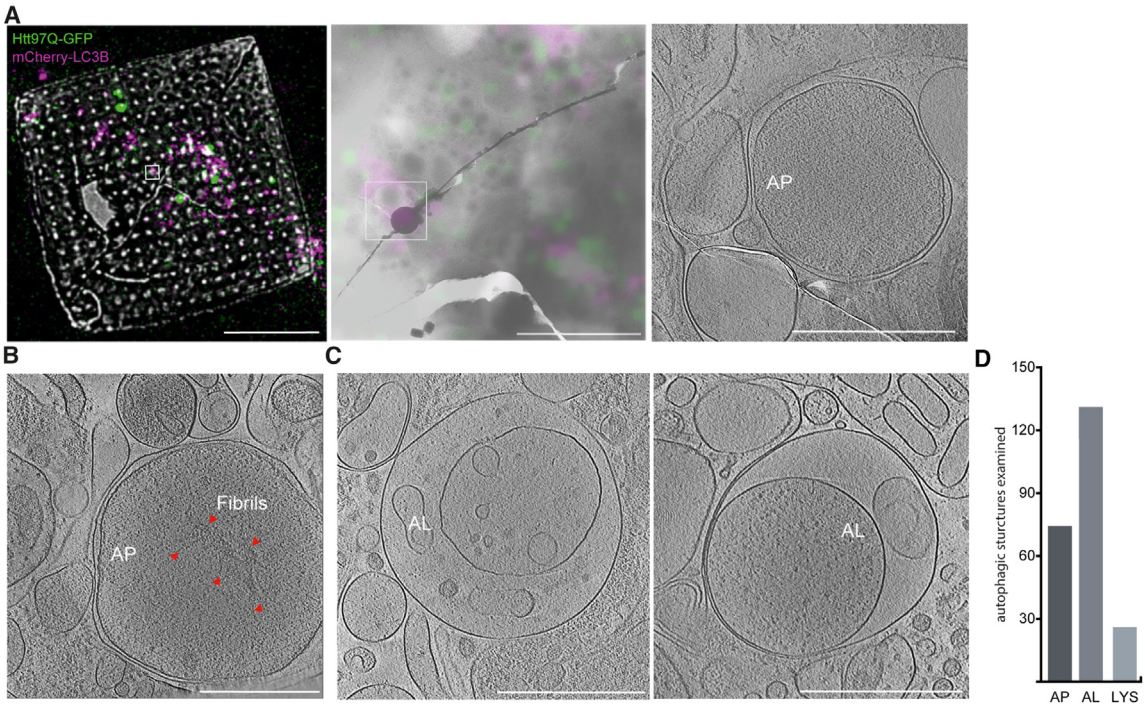

Figure 5. Autophagy preferentially targets the amorphous 97Q phase

(A) Left: A grid square of vitrified vesicles from mCherry-LC3B and 97Q-GFP co-expressed cells, imaged in the cryo-confocal microscope with the tomogram site boxed. Middle: cryo-TEM image (5,600x) with the corresponding tomogram site box overlayed with fluorescence. Right: tomographic slice (34,000x) with the GFP-positive autophagosome (AP) filled with amorphous content.

(B) A GFP-positive autophagosome that contains fibril-like structures.

(C) GFP-positive autolysosomes (AL) with amorphous content.

(D) Numbers of autophagic structures observed by cryo-ET upon isolation.

Scale bars: 10 μm (A left), 2 μm (A middle), 500 nm (A, B, and C tomographic slices).

size increase of the 97Q aggregates compared to control cells (Figure S13D). While Ub antibody stained both the peripheral region and the central zone of the polyQ aggregate upon immunofluorescence analysis (Figures S13E and S13F), p62 was only detected in the dim 64Q aggregates and the peripheral region around the 150Q or 97Q aggregates (Figures 4F and S13G), suggesting a specific interaction of p62 with the amorphous polyQ phase. To exclude an experimental bias due to antibody staining, we co-expressed a fluorescent-tagged version of p62, p62-RFP, confirming these observations (Figure S13H). The 64Q aggregates that interacted with p62 were indeed similar in GFP intensity to the 150Q peripheral region (Figures 4F and 4G), defining them as amorphous and thus amenable to aggrephagy through p62 binding. To further test the targeting of p62 to the amorphous polyQ, we isolated and partitioned cellular 64Q aggregates from cell lysates using filtration and subsequent enrichment by GFP pull-down. These experiments confirmed that p62 preferentially binds to the smaller aggregates but was not detected in the filter-trapped fraction (Figure 4H). Finally, siRNA knockdown of p62 in HEK293 cells (Figure S13I) consistently revealed an increase in the aggregate central zone and peripheral region (Figure S13J), coupled with a loss of LC3B and LysoTracker signals around the aggregates (Figure S13K). Knockdown of p62 resulted in a weaker phenotype than that of LC3A/B, likely indicating functional compensation due to receptor redundancy in the pathway. Collectively, these results demonstrate that p62 interacts with the amorphous non-fibrillar polyQ and mediates its intake into the phagophores.

Autophagosomes preferentially contain amorphous 97Q

Like all amyloids, polyQ fibrils consist of highly stable cross-β structures.[10,15,77] To provide further evidence that autophagosomes indeed preferentially engulf amorphous polyQ, we employed cryo-CLEM to examine the structural details of 97Q within autophagic vesicles. To this end, we plunge-froze the fluorescence-sorted mCherry/GFP double-positive vesicles (mCherry+/GFP+) isolated from 97Q/mCherry-LC3B-expressing HEK293 cells after induction of autophagy.[75] The vitrified vesicles were examined in a cryo-confocal fluorescence microscope to locate GFP and mCherry double-positive puncta; the z stacks containing the fluorescence signals were then correlated with the cryo-transmission electron microscope (TEM) overviews to locate the vesicle for tilt-series acquisition (Figure 5A). This analysis revealed different autophagic vesicles, ranging from bilamellar autophagosomes (Figures 5A, 5B, and S14A) to unilamellar autolysosomes (Figures 5C and S14B). From the 200 autophagic vesicles examined (Figure 5D), only one mCherry+/GFP+ autophagosome contained some fibrillar material of uncertain origin,

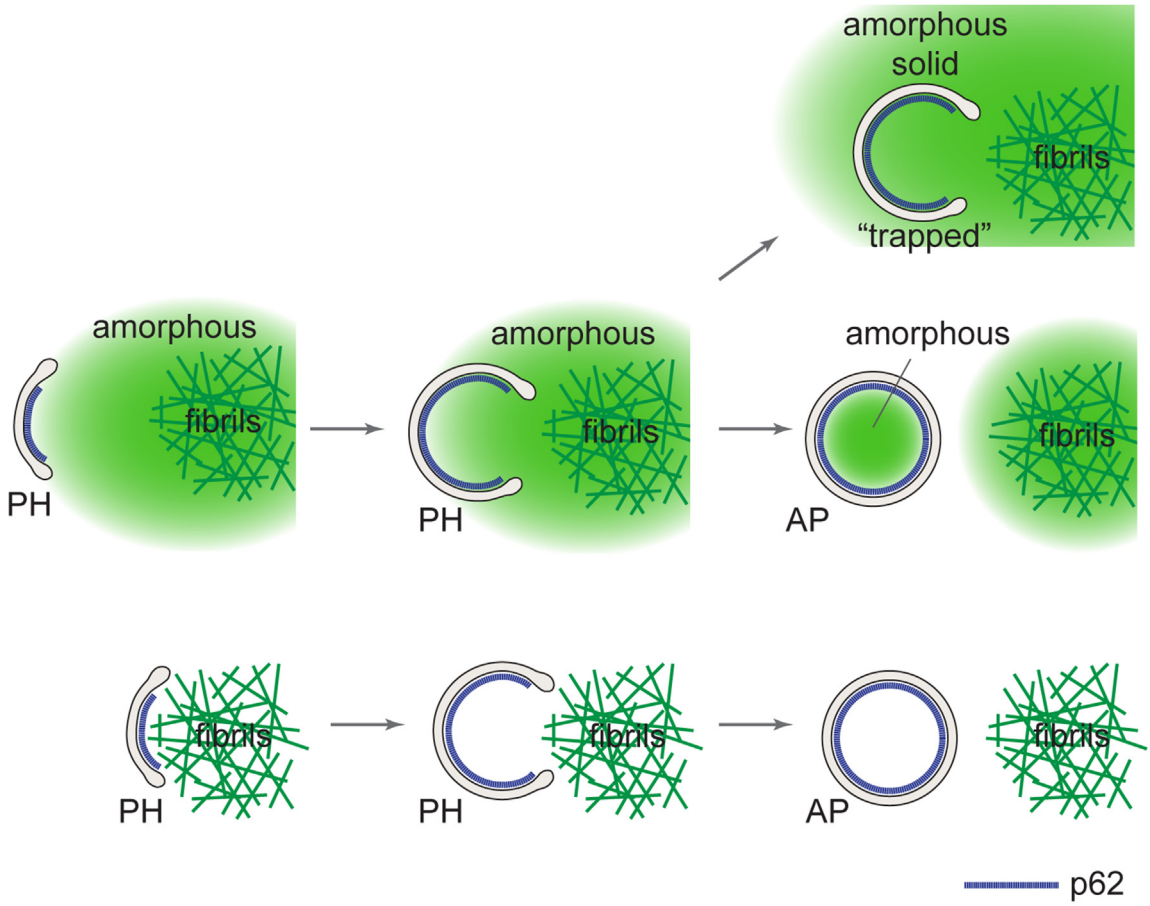

Figure 6. Model of p62-mediated autophagy of polyQ aggregates

Autophagy preferentially interacts with and engulfs the amorphous polyQ phase mediated by the autophagy receptor p62. Amyloid fibrils show no apparent engulfment by autophagy, and autophagic structures in close proximity are often observed to be cargo free. Both the fibrillar and the amorphous polyQ aggregates can trap phagophores (PH), leading to isolation and a block in phagophore maturation into autophagosomes (AP).

mixed with amorphous content (Figure 5B), while the rest of the autophagosomes and autolysosomes contained only amorphous density (examples in Figures 5A, 5C, S14A, and S14B).

Taken together, our results demonstrate that aggrephagy mediated by p62 preferentially targets amorphous rather than fibrillar polyQ aggregates.

DISCUSSION

The biogenesis of an autophagosome is a slow process that takes about 10 min.[78] During this time autophagic cargo must be concentrated and segregated into a distinct entity that can be engulfed by the autophagosomal membrane. Multiple interactions between autophagy receptors and Atg8/LC3/GABARAP family members are needed to establish a high-avidity interaction platform between the cargo and the phagophore, ensuring autophagosome biogenesis at the site of cargo recognition.[79] The physical properties of the cargo/receptor complex therefore should determine the efficiency of the autophagy process. In this study, we define the role of autophagy in polyQ degradation by visualizing polyQ aggregates within autophagosomes using cryo-CLEM. This structural analysis reveals that autophagy preferentially targets an amorphous polyQ phase rather than the fibrillar state (Figures 5A and 5B), proposing a model in which autophagy targets early stages of the polyQ aggregation pathway (Figure 6).

Recent reports have shown that various autophagic cargoes, together with their corresponding autophagy receptors, undergo co-condensate formation in the cytosol prior to autophagic engulfment,[80–83] highlighting a role of liquid-liquid phase separation in cargo recruitment. Furthermore, evidence has been presented that surface adhesion of liquid droplets to the phagophore membrane, also known as wetting,[84] is sufficient for liquid-like cargo/receptor condensate engulfment by phagophore membranes.[85] PolyQ aggregates initially exist in a liquid-like state but undergo a liquid-to-solid phase transition that shifts the equilibrium toward amyloid fibrils, with longer polyQ repeats undergoing more rapid transition.[19] Whether the amorphous polyQ aggregates that we identified as being degraded by autophagy are in a liquid-like or gel-like state remains to be determined. However, quantitative mass spectrometry experiments identified p62 as the major autophagy receptor in the

polyQ-containing autophagosomes (Figures 4D and 4E). p62 is a Ub-dependent autophagy receptor that forms phase-separated condensates in the presence of polyubiquitylated cargo molecules.[82,86,87] It is likely that targeting of p62 to the amorphous polyQ phase converts the polyQ aggregate to a more liquid-like state. Consistent with this hypothesis, FRAP analysis revealed a larger mobile fraction of 97Q within the amorphous polyQ phase when autophagy was activated by treh/rapa or torin1 or during LC3B overexpression, compared to LC3A/B knockout cells (Figure S2L). Fluorescence imaging showed that p62 localized exclusively to less concentrated polyQ aggregates, corresponding to the amorphous polyQ phase, and was excluded from the central zone of the aggregates despite being Ub positive (Figure 4G). In contrast, Ub was found in both the amorphous and fibrillar polyQ (Figures S13E and S13F). This behavior of p62 is consistent with previous reports,[88] but the molecular mechanism for the exclusion of p62 from the fibrillar polyQ pool remains to be determined. It is tempting to speculate that the multivalency of p62 and Ub, driving phase separation, cannot be established on the fibrils, because fibrils are poorly dynamic, and condensation in the amorphous polyQ phase sequesters p62 out of the fibrillar polyQ pool over time. Of note, modulation of autophagy affects both amorphous and fibrillar polyQ (Figure 2), consistent with the proposed transition of polyQ from a liquid to solid state with amyloid fibrils as the end product.

Recently, it has been shown that the aggregate surface is primed for p62 binding by the protein NEMO, which amplifies linear ubiquitination by the E3 ligase HOIP and generates a mobile, phase-separated aggregate surface.[89–91] Our mass spectrometry analysis of isolated autophagosomes did not identify NEMO, suggesting that its interaction with the aggregate surface may be transient. It is possible that modulation of the Ub chains further contributes to receptor-cargo interaction and productive autophagy initiation.

Among the various Ub-dependent autophagy receptors that function in selective autophagy, we find p62 to be of particular importance in polyQ aggrephagy, presumably based on its ability to phase-separate in the presence of ubiquitylated polyQ and from a link with the phagophore-conjugated LC3BII.[80–83,92] It is plausible that other receptors with domains important for oligomerization, such as TAX1BP1, NDP52, and NBR1,[93–95] also prefer droplet-like cargo assemblies with a “soft” surface in mediating selective autophagy. It has been shown that NBR1 enhances p62-Ub condensate formation and TAX1BP1 facilitates recruitment of the autophagy scaffold protein FIP200, suggesting that multiple factors may modulate the mobility of the amorphous polyQ phase.[82,86,96–98] A liquid-like state of the amorphous polyQ phase would provide a flexible surface for phagophore formation establishing high avidity, possibly resulting in piecemeal polyQ uptake (Figure 6), as seen previously for p62 droplets.[85] Such a mechanism would give rise to autophagosomes variable in size (Figure 3H) but generally much smaller than a full-sized aggregate deposit.

Contrary to a recent report,[73] our study does not support the proposed role of the chaperonin subunit CCT2 as a selective receptor of polyQ fibril aggrephagy. Specifically, we failed to obtain evidence by mass spectrometry for a specific enrichment of CCT2 in polyQ-containing autophagosomes. Moreover, our cryo-CLEM analysis provides no evidence that amyloid-like fibrils are the main target during aggrephagy. Only in a single case did we observe fibril-like structures, of uncertain origin, surrounded by amorphous density within a polyQ-positive autophagosome (Figure 5B). Nevertheless, our data raise the possibility that the fragmentation of fibrils by chaperones[33–35] and their partitioning into an amorphous phase may contribute to aggregate clearance via autophagy. It is also possible that the complete TRiC complex has a role in selective autophagy of polyQ aggregates.[99,100]

Our experiments also showed that aggrephagy is not always productive and often leads to the trapping of phagophore membranes within the amorphous polyQ phase (Figures S4H and S4I). The trapped double membrane structures do not show the characteristic features of phagophores and are frequently isolated from other organelles (Figures 3B–3G).[65,66] We speculate that the trapping of phagophores occurs due to a shift in polyQ material properties from liquid-like to solid during autophagosome biogenesis, incorporating the phagophore within the polyQ aggregate. Although the polyQ inclusions are apparently less toxic,[24,26] they contribute to cytopathology by sequestering key cellular proteins and physically affecting the integrity of membranes.[12,16] The ensnaring of autophagic structures within both the amorphous and fibrillar phases of the polyQ aggregates highlights the detrimental effect of aggregate formation on the proteostasis network. Impaired autophagy may contribute to the severe pathology of longer polyQ repeats that convert to fibrils more rapidly.[4,9] Thus the success of autophagy-based therapeutic interventions in polyQ diseases may depend on early detection prior to fibrillation or on ways to bypass a requirement for the Ub-p62 interaction.[101]

Limitations of the study

Due to technical limitations, we are unable to directly assay the autophagosome-encapsulated polyQ to unambiguously characterize its physical state. At present, we can only infer that the autophagosome-encapsulated polyQ is more soluble than solid amorphous or fibrillar aggregates from the observation that solid polyQ traps and arrests autophagosomes in an immature state. Our experiments also show that autophagy inhibition increases solidification of the amorphous polyQ pool. Furthermore, our resolutions do not allow us to determine if the autophagy-engulfed amorphous pool contains small fragments of fibrils or protofilaments, so we can’t exclude the possibility that at least some fibrillar polyQ is fragmented by chaperones prior to autophagic engulfment. The cell system we used in this study expresses the different polyQ versions from a strong promoter. It remains to be seen whether trapping of autophagic structures is similarly observed in patient-derived samples where polyQ aggregates accumulate over a long period of time.

STAR★METHODS

Detailed methods are provided in the online version of this paper and include the following:

- KEY RESOURCES TABLE
- RESOURCE AVAILABILITY
  - Lead contact

SUPPLEMENTAL INFORMATION

Supplemental information can be found online at https://doi.org/10.1016/j.molcel.2024.04.018.

ACKNOWLEDGMENTS

We acknowledge Martin Spitaler and Markus Oster at the MPI Imaging facility, and Dr. Barbara Steigenberger and Nicole Krombholz at the MPI Mass Spectrometry facility, and Dr. Tillman Schäffer and Dr. Daniel Bollschweiler at the MPI EM facility for technical support. We thank Dr. Dieter Edbauer for the p62-RFP construct. We acknowledge Jürgen Plitzko, Gopal Jayaraj, Hauke Holthusen, Victoria Trinkhaus, Rongqing Li, Hou Zhen, Florian Beck, Dustin Morado, Guenter Pfeifer, Matthias Poege, Meijing Li, Oda Schiøtz, Sven Klumpe, Anna Bieber, Christina Capitanio, and Inga Wolf for technical support. We acknowledge Brenda A. Schulman for discussions and advice on the study. D.Y.Z. acknowledges a postdoctoral fellowship funded by the Alexander von Humbolt Foundation. This study was supported by the Max-Planck-Gesellschaft and funded in part by Aligning Science Across Parkinson's (ASAP-000282) (Brenda A. Schulman, F.U.H., and W.B.) through the Michael J. Fox Foundation for Parkinson's Research (MJFF), the European Union (ERC, IntrinsicReceptors, 101041982), and the Deutsche Forschungsgemeinschaft (DFG, German Research Foundation) under Germany's Excellence Strategy (EXC 2067/1-390729940). Views and opinions expressed are those of the author(s) only and do not necessarily reflect those of the European Union or the European Research Council Executive Agency. Neither the European Union nor the granting authority can be held responsible for them. Open access funding enabled and organized by Projekt DEAL.

AUTHOR CONTRIBUTIONS

D.Y.Z., F.W., F.J.B.B., W.B., and F.U.H. designed the research project. W.B. provided instruments. D.Y.Z., F.J.B.B., and I.S. performed experiments with support from everyone. D.Y.Z., F.W., and F.U.H. wrote the manuscript with input from the other authors.

DECLARATION OF INTERESTS

The authors declare no competing interests.

Received: August 8, 2023
Revised: January 30, 2024
Accepted: April 23, 2024
Published: May 16, 2024

REFERENCES

1. Hipp, M.S., Kasturi, P., and Hartl, F.U. (2019). The proteostasis network and its decline in ageing. Nat. Rev. Mol. Cell Biol. *20*, 421–435.
2. Ross, C.A., and Poirier, M.A. (2004). Protein aggregation and neurodegenerative disease. Nat. Med. *10*, S10–S17.
3. Taylor, J.P., Hardy, J., and Fischbeck, K.H. (2002). Toxic proteins in neurodegenerative disease. Science *296*, 1991–1995.
4. Gusella, J.F., and MacDonald, M.E. (2006). Huntington's disease: seeing the pathogenic process through a genetic lens. Trends Biochem. Sci. *31*, 533–540.
5. Walker, F.O. (2007). Huntington's disease. Lancet *369*, 218–228.
6. Williams, A.J., and Paulson, H.L. (2008). Polyglutamine neurodegeneration: protein misfolding revisited. Trends Neurosci. *31*, 521–528.
7. Duyao, M., Ambrose, C., Myers, R., Novelletto, A., Persichetti, F., Frontali, M., Folstein, S., Ross, C., Franz, M., and Abbott, M. (1993). Trinucleotide repeat length instability and age of onset in Huntington's disease. Nat. Genet. *4*, 387–392.
8. Group, T.H.s.D.C.R. (1993). A novel gene containing a trinucleotide repeat that is expanded and unstable on Huntington's disease chromosomes. Cell *72*, 971–983.
9. DiFiglia, M., Sapp, E., Chase, K.O., Davies, S.W., Bates, G.P., Vonsattel, J.P., and Aronin, N. (1997). Aggregation of huntingtin in neuronal intranuclear inclusions and dystrophic neurites in brain. Science *277*, 1990–1993.
10. Scherzinger, E., Lurz, R., Turmaine, M., Mangiarini, L., Hollenbach, B., Hasenbank, R., Bates, G.P., Davies, S.W., Lehrach, H., and Wanker, E.E. (1997). Huntingtin-encoded polyglutamine expansions form amyloid-like protein aggregates in vitro and in vivo. Cell *90*, 549–558.
11. Bäuerlein, F.J.B., Fernández-Busnadiego, R., and Baumeister, W. (2020). Investigating the Structure of Neurotoxic Protein Aggregates Inside Cells. Trends Cell Biol. *30*, 951–966.
12. Bäuerlein, F.J.B., Saha, I., Mishra, A., Kalemanov, M., Martínez-Sánchez, A., Klein, R., Dudanova, I., Hipp, M.S., Hartl, F.U., Baumeister, W., and Fernández-Busnadiego, R. (2017). In Situ Architecture and Cellular Interactions of PolyQ Inclusions. Cell *171*, 179–187.e10.
13. Chiti, F., and Dobson, C.M. (2017). Protein Misfolding, Amyloid Formation, and Human Disease: A Summary of Progress Over the Last Decade. Annu. Rev. Biochem. *86*, 27–68.
14. Gruber, A., Hornburg, D., Antonin, M., Krahmer, N., Collado, J., Schaffer, M., Zubaite, G., Lüchtenborg, C., Sachsenheimer, T., Brügger, B., et al. (2018). Molecular and structural architecture of polyQ aggregates in yeast. Proc. Natl. Acad. Sci. USA *115*, E3446–E3453.
15. Hoop, C.L., Lin, H.K., Kar, K., Magyarfalvi, G., Lamley, J.M., Boatz, J.C., Mandal, A., Lewandowski, J.R., Wetzel, R., and van der Wel, P.C.A. (2016). Huntingtin exon 1 fibrils feature an interdigitated β-hairpin-based polyglutamine core. Proc. Natl. Acad. Sci. USA *113*, 1546–1551.
16. Kim, Y.E., Hosp, F., Frottin, F., Ge, H., Mann, M., Hayer-Hartl, M., and Hartl, F.U. (2016). Soluble Oligomers of PolyQ-Expanded Huntingtin Target a Multiplicity of Key Cellular Factors. Mol. Cell *63*, 951–964.
17. Miller, J., Arrasate, M., Brooks, E., Libeu, C.P., Legleiter, J., Hatters, D., Curtis, J., Cheung, K., Krishnan, P., Mitra, S., et al. (2011). Identifying polyglutamine protein species in situ that best predict neurodegeneration. Nat. Chem. Biol. *8*, 318.
18. Nucifora, L.G., Burke, K.A., Feng, X., Arbez, N., Zhu, S., Miller, J., Yang, G., Ratovitski, T., Delannoy, M., Muchowski, P.J., et al. (2012). Identification of novel potentially toxic oligomers formed in vitro from mammalian-derived expanded huntingtin exon-1 protein. J. Biol. Chem. *287*, 16017–16028.
19. Peskett, T.R., Rau, F., O'Driscoll, J., Patani, R., Lowe, A.R., and Saibil, H.R. (2018). A Liquid to Solid Phase Transition Underlying Pathological Huntingtin Exon1 Aggregation. Mol. Cell *70*, 588–601.e6.
20. Bennett, E.J., Bence, N.F., Jayakumar, R., and Kopito, R.R. (2005). Global impairment of the ubiquitin-proteasome system by nuclear or cytoplasmic protein aggregates precedes inclusion body formation. Mol. Cell *17*, 351–365.

21. Leitman, J., Ulrich Hartl, F., and Lederkremer, G.Z. (2013). Soluble forms of polyQ-expanded huntingtin rather than large aggregates cause endoplasmic reticulum stress. Nat. Commun. *4*, 2753.

22. Park, S.H., Kukushkin, Y., Gupta, R., Chen, T., Konagai, A., Hipp, M.S., Hayer-Hartl, M., and Hartl, F.U. (2013). PolyQ Proteins Interfere with Nuclear Degradation of Cytosolic Proteins by Sequestering the Sis1p Chaperone. Cell *154*, 134–145.

23. Schaffar, G., Breuer, P., Boteva, R., Behrends, C., Tzvetkov, N., Strippel, N., Sakahira, H., Siegers, K., Hayer-Hartl, M., and Hartl, F.U. (2004). Cellular toxicity of polyglutamine expansion proteins: mechanism of transcription factor deactivation. Mol Cell. *15*, 95–105.

24. Arrasate, M., Mitra, S., Schweitzer, E.S., Segal, M.R., and Finkbeiner, S. (2004). Inclusion body formation reduces levels of mutant huntingtin and the risk of neuronal death. Nature *431*, 805–810.

25. Arrasate, M., and Finkbeiner, S. (2012). Protein aggregates in Huntington's disease. Exp. Neurol. *238*, 1–11.

26. Slow, E.J., Graham, R.K., Osmand, A.P., Devon, R.S., Lu, G., Deng, Y., Pearson, J., Vaid, K., Bissada, N., Wetzel, R., et al. (2005). Absence of behavioral abnormalities and neurodegeneration in vivo despite widespread neuronal huntingtin inclusions. Proc. Natl. Acad. Sci. USA *102*, 11402–11407.

27. Sánchez, I., Mahlke, C., and Yuan, J. (2003). Pivotal role of oligomerization in expanded polyglutamine neurodegenerative disorders. Nature *421*, 373–379.

28. Bence, N.F., Sampat, R.M., and Kopito, R.R. (2001). Impairment of the ubiquitin-proteasome system by protein aggregation. Science *292*, 1552–1555.

29. Guo, Q., Lehmer, C., Martínez-Sánchez, A., Rudack, T., Beck, F., Hartmann, H., Pérez-Berlanga, M., Frottin, F., Hipp, M.S., Hartl, F.U., et al. (2018). In Situ Structure of Neuronal C9orf72 Poly-GA Aggregates Reveals Proteasome Recruitment. Cell *172*, 696–705.e12.

30. Holmberg, C.I., Staniszewski, K.E., Mensah, K.N., Matouschek, A., and Morimoto, R.I. (2004). Inefficient degradation of truncated polyglutamine proteins by the proteasome. EMBO J. *23*, 4307–4318.

31. Venkatraman, P., Wetzel, R., Tanaka, M., Nukina, N., and Goldberg, A.L. (2004). Eukaryotic proteasomes cannot digest polyglutamine sequences and release them during degradation of polyglutamine-containing proteins. Mol. Cell *14*, 95–104.

32. Verhoef, L.G.G.C., Lindsten, K., Masucci, M.G., and Dantuma, N.P. (2002). Aggregate formation inhibits proteasomal degradation of polyglutamine proteins. Hum. Mol. Genet. *11*, 2689–2700.

33. Nillegoda, N.B., Wentink, A.S., and Bukau, B. (2018). Protein Disaggregation in Multicellular Organisms. Trends Biochem. Sci. *43*, 285–300.

34. Saha, I., Yuste-Checa, P., Da Silva Padilha, M., Guo, Q., Körner, R., Holthusen, H., Trinkaus, V.A., Dudanova, I., Fernández-Busnadiego, R., Baumeister, W., et al. (2023). The AAA+ chaperone VCP disaggregates Tau fibrils and generates aggregate seeds in a cellular system. Nat. Commun. *14*, 560.

35. Tyedmers, J., Mogk, A., and Bukau, B. (2010). Cellular strategies for controlling protein aggregation. Nat. Rev. Mol. Cell Biol. *11*, 777–788.

36. Hara, T., Nakamura, K., Matsui, M., Yamamoto, A., Nakahara, Y., Suzuki-Migishima, R., Yokoyama, M., Mishima, K., Saito, I., Okano, H., and Mizushima, N. (2006). Suppression of basal autophagy in neural cells causes neurodegenerative disease in mice. Nature *441*, 885–889.

37. Iwata, A., Christianson, J.C., Bucci, M., Ellerby, L.M., Nukina, N., Forno, L.S., and Kopito, R.R. (2005). Increased susceptibility of cytoplasmic over nuclear polyglutamine aggregates to autophagic degradation. Proc. Natl. Acad. Sci. USA *102*, 13135–13140.

38. Komatsu, M., Waguri, S., Chiba, T., Murata, S., Iwata, J., Tanida, I., Ueno, T., Koike, M., Uchiyama, Y., Kominami, E., and Tanaka, K. (2006). Loss of autophagy in the central nervous system causes neurodegeneration in mice. Nature *441*, 880–884.

39. Leeman, D.S., Hebestreit, K., Ruetz, T., Webb, A.E., McKay, A., Pollina, E.A., Dulken, B.W., Zhao, X., Yeo, R.W., Ho, T.T., et al. (2018). Lysosome activation clears aggregates and enhances quiescent neural stem cell activation during aging. Science *359*, 1277–1283.

40. Mizushima, N. (2018). A brief history of autophagy from cell biology to physiology and disease. Nat. Cell Biol. *20*, 521–527.

41. Ravikumar, B. (2002). Aggregate-prone proteins with polyglutamine and polyalanine expansions are degraded by autophagy. Hum. Mol. Genet. *11*, 1107–1117.

42. Deng, Z., Purtell, K., Lachance, V., Wold, M.S., Chen, S., and Yue, Z. (2017). Autophagy Receptors and Neurodegenerative Diseases. Trends Cell Biol. *27*, 491–504.

43. Hjerpe, R., Bett, J.S., Keuss, M.J., Solovyova, A., McWilliams, T.G., Johnson, C., Sahu, I., Varghese, J., Wood, N., Wightman, M., et al. (2016). UBQLN2 Mediates Autophagy-Independent Protein Aggregate Clearance by the Proteasome. Cell *166*, 935–949.

44. Levine, B., and Kroemer, G. (2019). Biological Functions of Autophagy Genes: A Disease Perspective. Cell *176*, 11–42.

45. Nixon, R.A. (2013). The role of autophagy in neurodegenerative disease. Nat. Med. *19*, 983–997.

46. Stamatakou, E., Wróbel, L., Hill, S.M., Puri, C., Son, S.M., Fujimaki, M., Zhu, Y., Siddiqi, F., Fernandez-Estevez, M., Manni, M.M., et al. (2020). Mendelian neurodegenerative disease genes involved in autophagy. Cell Discovery *6*, 24.

47. Boland, B., Yu, W.H., Corti, O., Mollereau, B., Henriques, A., Bezard, E., Pastores, G.M., Rubinsztein, D.C., Nixon, R.A., Duchen, M.R., et al. (2018). Promoting the clearance of neurotoxic proteins in neurodegenerative disorders of ageing. Nat. Rev. Drug Discov. *17*, 660–688.

48. Hansen, M., Rubinsztein, D.C., and Walker, D.W. (2018). Autophagy as a promoter of longevity: insights from model organisms. Nat. Rev. Mol. Cell Biol. *19*, 579–593.

49. Rubinsztein, D.C., Mariño, G., and Kroemer, G. (2011). Autophagy and aging. Cell *146*, 682–695.

50. Ashkenazi, A., Bento, C.F., Ricketts, T., Vicinanza, M., Siddiqi, F., Pavel, M., Squitieri, F., Hardenberg, M.C., Imarisio, S., Menzies, F.M., and Rubinsztein, D.C. (2017). Polyglutamine tracts regulate beclin 1-dependent autophagy. Nature *545*, 108–111.

51. Sarkar, S., Davies, J.E., Huang, Z., Tunnacliffe, A., and Rubinsztein, D.C. (2007). Trehalose, a novel mTOR-independent autophagy enhancer, accelerates the clearance of mutant huntingtin and α-synuclein. J. Biol. Chem. *282*, 5641–5652.

52. Sap, K.A., Guler, A.T., Bezstarosti, K., Bury, A.E., Juenemann, K., Demmers, J.A., and Reits, E.A. (2019). Global Proteome and Ubiquitinome Changes in the Soluble and Insoluble Fractions of Q175 Huntington Mice Brains. Mol. Cell. Proteomics *18*, 1705–1720.

53. Bjorkoy, G., Lamark, T., Brech, A., Outzen, H., Perander, M., Overvatn, A., Stenmark, H., and Johansen, T. (2005). p62/SQSTM1 forms protein aggregates degraded by autophagy and has a protective effect on huntingtin-induced cell death. J. Cell Biol. *171*, 603–614.

54. Wurzer, B., Zaffagnini, G., Fracchiolla, D., Turco, E., Abert, C., Romanov, J., and Martens, S. (2015). Oligomerization of p62 allows for selection of ubiquitinated cargo and isolation membrane during selective autophagy. Elife *4*, e08941.

55. Kim, J., Kundu, M., Viollet, B., and Guan, K.L. (2011). AMPK and mTOR regulate autophagy through direct phosphorylation of Ulk1. Nat. Cell Biol. *13*, 132–141.

56. Rusmini, P., Cortese, K., Crippa, V., Cristofani, R., Cicardi, M.E., Ferrari, V., Vezzoli, G., Tedesco, B., Meroni, M., Messi, E., et al. (2019). Trehalose induces autophagy via lysosomal-mediated TFEB activation in models of motoneuron degeneration. Autophagy *15*, 631–651.

57. Tanaka, M., Machida, Y., Niu, S., Ikeda, T., Jana, N.R., Doi, H., Kurosawa, M., Nekooki, M., and Nukina, N. (2004). Trehalose alleviates

polyglutamine-mediated pathology in a mouse model of Huntington disease. Nat. Med. *10*, 148–154.

58. Shoji-Kawata, S., Sumpter, R., Leveno, M., Campbell, G.R., Zou, Z., Kinch, L., Wilkins, A.D., Sun, Q., Pallauf, K., MacDuff, D., et al. (2013). Identification of a candidate therapeutic autophagy-inducing peptide. Nature *494*, 201–206.
59. Wang, G.H., Mitsui, K., Kotliarova, S., Yamashita, A., Nagao, Y., Tokuhiro, S., Iwatsubo, T., Kanazawa, I., and Nukina, N. (1999). Caspase activation during apoptotic cell death induced by expanded polyglutamine in N2a cells. Neuroreport *10*, 2435–2438.
60. Mauthe, M., Orhon, I., Rocchi, C., Zhou, X., Luhr, M., Hijlkema, K.J., Coppes, R.P., Engedal, N., Mari, M., and Reggiori, F. (2018). Chloroquine inhibits autophagic flux by decreasing autophagosome-lysosome fusion. Autophagy *14*, 1435–1455.
61. Hyer, M.L., Milhollen, M.A., Ciavarri, J., Fleming, P., Traore, T., Sappal, D., Huck, J., Shi, J., Gavin, J., Brownell, J., et al. (2018). A small-molecule inhibitor of the ubiquitin activating enzyme for cancer treatment. Nat. Med. *24*, 186–193.
62. Arnold, J., Mahamid, J., Lucic, V., de Marco, A., Fernandez, J.J., Laugks, T., Mayer, T., Hyman, A.A., Baumeister, W., and Plitzko, J.M. (2016). Site-Specific Cryo-focused Ion Beam Sample Preparation Guided by 3D Correlative Microscopy. Biophys. J. *110*, 860–869.
63. Goetz, S.K., and Mahamid, J. (2020). Visualizing Molecular Architectures of Cellular Condensates: Hints of Complex Coacervation Scenarios. Dev. Cell *55*, 97–107.
64. Schorb, M., Gaechter, L., Avinoam, O., Sieckmann, F., Clarke, M., Bebeacua, C., Bykov, Y.S., Sonnen, A.F.P., Lihl, R., and Briggs, J.A.G. (2017). New hardware and workflows for semi-automated correlative cryo-fluorescence and cryo-electron microscopy/tomography. J. Struct. Biol. *197*, 83–93.
65. Bieber, A., Capitanio, C., Erdmann, P.S., Fiedler, F., Beck, F., Lee, C.W., Li, D., Hummer, G., Schulman, B.A., Baumeister, W., and Wilfling, F. (2022). In situ structural analysis reveals membrane shape transitions during autophagosome formation. Proc. Natl. Acad. Sci. USA *119*, e2209823119.
66. Li, M., Tripathi-Giesgen, I., Schulman, B.A., Baumeister, W., and Wilfling, F. (2023). In situ snapshots along a mammalian selective autophagy pathway. Proc. Natl. Acad. Sci. USA *120*, e2221712120.
67. Lee, H.J., Yoon, Y.S., and Lee, S.J. (2018). Mechanism of neuroprotection by trehalose: controversy surrounding autophagy induction. Cell Death Dis. *9*, 712.
68. Crowe, J.H. (2007). Trehalose as a "chemical chaperone": fact and fantasy. Adv. Exp. Med. Biol. *594*, 143–158.
69. Schindelin, J., Arganda-Carreras, I., Frise, E., Kaynig, V., Longair, M., Pietzsch, T., Preibisch, S., Rueden, C., Saalfeld, S., Schmid, B., et al. (2012). Fiji: an open-source platform for biological-image analysis. Nat. Methods *9*, 676–682.
70. Weidberg, H., Shpilka, T., Shvets, E., Abada, A., Shimron, F., and Elazar, Z. (2011). LC3 and GATE-16 N termini mediate membrane fusion processes required for autophagosome biogenesis. Dev. Cell *20*, 444–454.
71. Carter, S.D., Mamede, J.I., Hope, T.J., and Jensen, G.J. (2020). Correlated cryogenic fluorescence microscopy and electron cryo-tomography shows that exogenous TRIM5alpha can form hexagonal lattices or autophagy aggregates in vivo. Proc. Natl. Acad. Sci. USA *117*, 29702–29711.
72. Kaizuka, T., Morishita, H., Hama, Y., Tsukamoto, S., Matsui, T., Toyota, Y., Kodama, A., Ishihara, T., Mizushima, T., and Mizushima, N. (2016). An Autophagic Flux Probe that Releases an Internal Control. Mol. Cell *64*, 835–849.
73. Ma, X., Lu, C., Chen, Y., Li, S., Ma, N., Tao, X., Li, Y., Wang, J., Zhou, M., Yan, Y.B., et al. (2022). CCT2 is an aggrephagy receptor for clearance of solid protein aggregates. Cell *185*, 1325–1345.e22.
74. Cox, J., Hein, M.Y., Luber, C.A., Paron, I., Nagaraj, N., and Mann, M. (2014). Accurate proteome-wide label-free quantification by delayed normalization and maximal peptide ratio extraction, termed MaxLFQ. Mol. Cell. Proteomics *13*, 2513–2526.
75. Gao, W., Kang, J.H., Liao, Y., Ding, W.X., Gambotto, A.A., Watkins, S.C., Liu, Y.J., Stolz, D.B., and Yin, X.M. (2010). Biochemical isolation and characterization of the tubulovesicular LC3-positive autophagosomal compartment. J. Biol. Chem. *285*, 1371–1383.
76. Kato, M., Han, T.W., Xie, S., Shi, K., Du, X., Wu, L.C., Mirzaei, H., Goldsmith, E.J., Longgood, J., Pei, J., et al. (2012). Cell-free formation of RNA granules: low complexity sequence domains form dynamic fibers within hydrogels. Cell *149*, 753–767.
77. Perutz, M.F., Johnson, T., Suzuki, M., and Finch, J.T. (1994). Glutamine repeats as polar zippers: Their possible role in inherited neurodegenerative diseases. Proc. Natl. Acad. Sci. USA *91*, 5355–5358.
78. Geng, J., Baba, M., Nair, U., and Klionsky, D.J. (2008). Quantitative analysis of autophagy-related protein stoichiometry by fluorescence microscopy. J. Cell Biol. *182*, 129–140.
79. Kirkin, V., and Rogov, V.V. (2019). A Diversity of Selective Autophagy Receptors Determines the Specificity of the Autophagy Pathway. Mol. Cell *76*, 268–285.
80. Wilfling, F., Lee, C.W., Erdmann, P.S., Zheng, Y., Sherpa, D., Jentsch, S., Pfander, B., Schulman, B.A., and Baumeister, W. (2020). A Selective Autophagy Pathway for Phase-Separated Endocytic Protein Deposits. Mol. Cell *80*, 764–778.e7.
81. Yamasaki, A., Alam, J.M., Noshiro, D., Hirata, E., Fujioka, Y., Suzuki, K., Ohsumi, Y., and Noda, N.N. (2020). Liquidity Is a Critical Determinant for Selective Autophagy of Protein Condensates. Mol. Cell *77*, 1163–1175.e9.
82. Zaffagnini, G., Savova, A., Danieli, A., Romanov, J., Tremel, S., Ebner, M., Peterbauer, T., Sztacho, M., Trapannone, R., Tarafder, A.K., et al. (2018). p62 filaments capture and present ubiquitinated cargos for autophagy. EMBO J. *37*, e98308.
83. Zhang, G., Wang, Z., Du, Z., and Zhang, H. (2018). mTOR Regulates Phase Separation of PGL Granules to Modulate Their Autophagic Degradation. Cell *174*, 1492–1506.e1422.
84. Mangiarotti, A., Chen, N., Zhao, Z., Lipowsky, R., and Dimova, R. (2023). Wetting and complex remodeling of membranes by biomolecular condensates. Nat. Commun. *14*, 2809.
85. Agudo-Canalejo, J., Schultz, S.W., Chino, H., Migliano, S.M., Saito, C., Koyama-Honda, I., Stenmark, H., Brech, A., May, A.I., Mizushima, N., and Knorr, R.L. (2021). Wetting regulates autophagy of phase-separated compartments and the cytosol. Nature *591*, 142–146.
86. Jakobi, A.J., Huber, S.T., Mortensen, S.A., Schultz, S.W., Palara, A., Kuhm, T., Shrestha, B.K., Lamark, T., Hagen, W.J.H., Wilmanns, M., et al. (2020). Structural basis of p62/SQSTM1 helical filaments and their role in cellular cargo uptake. Nat. Commun. *11*, 440.
87. Sun, D., Wu, R., Zheng, J., Li, P., and Yu, L. (2018). Polyubiquitin chain-induced p62 phase separation drives autophagic cargo segregation. Cell Res. *28*, 405–415.
88. Bjørkøy, G., Lamark, T., Brech, A., Outzen, H., Perander, M., Overvatn, A., Stenmark, H., and Johansen, T. (2005). p62/SQSTM1 forms protein aggregates degraded by autophagy and has a protective effect on huntingtin-induced cell death. J. Cell Biol. 2005 *171*, 603–614.
89. Goel, S., Oliva, R., Jeganathan, S., Bader, V., Krause, L.J., Kriegler, S., Stender, I.D., Christine, C.W., Nakamura, K., Hoffmann, J.E., et al. (2023). Linear ubiquitination induces NEMO phase separation to activate NF-kappaB signaling. Life Sci. Alliance *6*.
90. van Well, E.M., Bader, V., Patra, M., Sánchez-Vicente, A., Meschede, J., Furthmann, N., Schnack, C., Blusch, A., Longworth, J., Petrasch-Parwez, E., et al. (2019). A protein quality control pathway regulated by linear ubiquitination. EMBO J. *38*, e100730.

91. Furthmann, N., Bader, V., Angersbach, L., Blusch, A., Goel, S., Sánchez-Vicente, A., Krause, L.J., Chaban, S.A., Grover, P., Trinkaus, V.A., et al. (2023). NEMO reshapes the alpha-Synuclein aggregate interface and acts as an autophagy adapter by co-condensation with p62. Nat. Commun. *14*, 8368.

92. Bjorkoy, G., Lamark, T., and Johansen, T. (2006). p62/SQSTM1: a missing link between protein aggregates and the autophagy machinery. Autophagy *2*, 138–139.

93. Kirkin, V., Lamark, T., Johansen, T., and Dikic, I. (2009). NBR1 cooperates with p62 in selective autophagy of ubiquitinated targets. Autophagy *5*, 732–733.

94. Lu, K., Den Brave, F., and Jentsch, S. (2017). Receptor oligomerization guides pathway choice between proteasomal and autophagic degradation. Nat. Cell Biol. *19*, 732–739.

95. Nthiga, T.M., Shrestha, B.K., Bruun, J.A., Larsen, K.B., Lamark, T., and Johansen, T. (2021). Regulation of Golgi turnover by CALCOCO1-mediated selective autophagy. J. Cell Biol. *220*, e202006128.

96. Kirkin, V., Lamark, T., Sou, Y.S., Bjørkøy, G., Nunn, J.L., Bruun, J.A., Shvets, E., McEwan, D.G., Clausen, T.H., Wild, P., et al. (2009). A role for NBR1 in autophagosomal degradation of ubiquitinated substrates. Mol. Cell *33*, 505–516.

97. Sánchez-Martín, P., Sou, Y.S., Kageyama, S., Koike, M., Waguri, S., and Komatsu, M. (2020). NBR1-mediated p62-liquid droplets enhance the Keap1-Nrf2 system. EMBO Rep. *21*, e48902.

98. Turco, E., Savova, A., Gere, F., Ferrari, L., Romanov, J., Schuschnig, M., and Martens, S. (2021). Reconstitution defines the roles of p62, NBR1 and TAX1BP1 in ubiquitin condensate formation and autophagy initiation. Nat. Commun. *12*, 5212.

99. Pavel, M., Imarisio, S., Menzies, F.M., Jimenez-Sanchez, M., Siddiqi, F.H., Wu, X., Renna, M., O'Kane, C.J., Crowther, D.C., and Rubinsztein, D.C. (2016). CCT complex restricts neuropathogenic protein aggregation via autophagy. Nat. Commun. *7*, 13821.

100. Tam, S., Geller, R., Spiess, C., and Frydman, J. (2006). The chaperonin TRiC controls polyglutamine aggregation and toxicity through subunit-specific interactions. Nat. Cell Biol. *8*, 1155–1162.

101. Li, Z., Wang, C., Wang, Z., et al. (2019). Allele-selective lowering of mutant HTT protein by HTT–LC3 linker compounds. Nature *575*, 203–209. https://doi.org/10.1038/s41586-019-1722-1.

102. Woerner, A.C., Frottin, F., Hornburg, D., Feng, L.R., Meissner, F., Patra, M., Tatzelt, J., Mann, M., Winklhofer, K.F., Hartl, F.U., and Hipp, M.S. (2016). Cytoplasmic protein aggregates interfere with nucleocytoplasmic transport of protein and RNA. Science *351*, 173–176.

103. Koulouras, G., Panagopoulos, A., Rapsomaniki, M.A., Giakoumakis, N.N., Taraviras, S., and Lygerou, Z. (2018). EasyFRAP-web: a web-based tool for the analysis of fluorescence recovery after photobleaching data. Nucleic Acids Res. *46*, W467–W472.

104. Cox, J., and Mann, M. (2008). MaxQuant enables high peptide identification rates, individualized p.p.b.-range mass accuracies and proteome-wide protein quantification. Nat. Biotechnol. *26*, 1367–1372.

105. Mastronarde, D.N. (2005). Automated electron microscope tomography using robust prediction of specimen movements. J. Struct. Biol. *152*, 36–51.

106. Zheng, S.Q., Palovcak, E., Armache, J.P., Verba, K.A., Cheng, Y., and Agard, D.A. (2017). MotionCor2: anisotropic correction of beam-induced motion for improved cryo-electron microscopy. Nat. Methods *14*, 331–332.

107. Grant, T., and Grigorieff, N. (2015). Measuring the optimal exposure for single particle cryo-EM using a 2.6 A reconstruction of rotavirus VP6. Elife *4*, e06980.

108. Kremer, J.R., Mastronarde, D.N., and McIntosh, J.R. (1996). Computer visualization of three-dimensional image data using IMOD. J. Struct. Biol. *116*, 71–76.

109. Rigort, A., Günther, D., Hegerl, R., Baum, D., Weber, B., Prohaska, S., Medalia, O., Baumeister, W., and Hege, H.C. (2012). Automated segmentation of electron tomograms for a quantitative description of actin filament networks. J. Struct. Biol. *177*, 135–144.

110. Salfer, M., Collado, J.F., Baumeister, W., Fernández-Busnadiego, R., and Martínez-Sánchez, A. (2020). Reliable estimation of membrane curvature for cryo-electron tomography. PLoS Comput. Biol. *16*, e1007962.

111. Martinez-Sanchez, A., Garcia, I., Asano, S., Lucic, V., and Fernandez, J.J. (2014). Robust membrane detection based on tensor voting for electron tomography. J. Struct. Biol. *186*, 49–61.

112. Nickell, S., Förster, F., Linaroudis, A., Net, W.D., Beck, F., Hegerl, R., Baumeister, W., and Plitzko, J.M. (2005). TOM software toolbox: acquisition and analysis for electron tomography. J. Struct. Biol. *149*, 227–234.

113. Hrabe, T., Chen, Y., Pfeffer, S., Cuellar, L.K., Mangold, A.V., and Förster, F. (2012). PyTom: a python-based toolbox for localization of macromolecules in cryo-electron tomograms and subtomogram analysis. J. Struct. Biol. *178*, 177–188.

114. Bäuerlein, F.J., Pastor-Pareja, J.C., and Fernández-Busnadiego, R. (2022). Cryo-electron tomography of native Drosophila tissues vitrified by plunge freezing. Preprint at bioRxiv. https://doi.org/10.1101/2021.04.14.437159.

115. Buchholz, T.O., Krull, A., Shahidi, R., Pigino, G., Jékely, G., and Jug, F. (2019). Content-aware image restoration for electron microscopy. Methods Cell Biol. *152*, 277–289.

116. Bepler, T., Kelley, K., Noble, A.J., and Berger, B. (2020). Topaz-Denoise: general deep denoising models for cryoEM and cryoET. Nat. Commun. *11*, 5208.

117. Fernandez, J.J., Laugks, U., Schaffer, M., Bäuerlein, F.J.B., Khoshouei, M., Baumeister, W., and Lucic, V. (2016). Removing Contamination-Induced Reconstruction Artifacts from Cryo-electron Tomograms. Biophys. J. *110*, 850–859.

118. Schwanhäusser, B., Busse, D., Li, N., Dittmar, G., Schuchhardt, J., Wolf, J., Chen, W., and Selbach, M. (2011). Global quantification of mammalian gene expression control. Nature *473*, 337–342.

STAR★METHODS

KEY RESOURCES TABLE

REAGENT or RESOURCE	SOURCE	IDENTIFIER
Antibodies		
Mouse anti-myc	Millipore	#05–724, (RRID:AB_309938)
Mouse anti-actin	Abcepta	#P60709, (RRID:AB_10664137)
Mouse anti-VCP	Abcam	#ab11433 (RRID:AB_298039)
Rabbit anti-MAP1LC3B	Novusbio	#NB100-222-s (RRID:AB_10003146)
Rabbit anti-MAP1LC3B	Santa Cruz	#sc-376404 (RRID:AB_11150489)
Rabbit anti-MAP1LC3B	Sigma-Aldrich	#L7543 (RRID:AB_796155)
Mouse anti-tubulin	Sigma-Aldrich	#T6199 (RRID:AB_477583)
Rabbit anti-p62	Enzo	#BML-PW9860 (RRID:AB_2196009)
Mouse anti-ubiquitin	Santa Cruz	#sc-8017 (RRID:AB_628423)
Mouse anti-polyQ	Sigma-Aldrich	#MABN821 (RRID:AB_2920696)
Mouse anti-GFP	Santa Cruz	#sc9996 (RRID:AB_627695)
Rabbit anti-GFP	Roche	#11814460001(RRID:AB_390913)
Goat anti-rabbit HRP	Sigma-Aldrich	#A9169 (RRID:AB_258434)
Goat anti-mouse HRP	Sigma-Aldrich	#A4416 (RRID:AB_258167)
Goat anti-mouse CF350	Sigma-Aldrich	#SAB4600013 (RRID:AB_3095587)
Goat anti-rabbit 555	Thermo Fisher Scientific	#A-21428 (RRID:AB_2535849)
Chemicals, peptides, and recombinant proteins		
Hochest	Cell signaling,	#33342
ER Tracker Red	Invitrogen	#E34250
LysoTracker red DND-99	Invitrogen	#L7528
Janelia Fluor 549 HaloTag Ligand	Promega	#GA1111
Annexin V pacific blue	Invitrogen	#R37177
Annexin V iFlour 555	Abcam	#ab219905
Lipofectamine 3000	Invitrogen	#L3000001
Fluoromount	Sigma-Aldrich	#F4680
Muristerone A	Abcam	#ab144309
rapamycin	AdipoGen	#AG-CN2
trehalose dihydrate	Sigma-Aldrich	#T9531
torin1	Selleckchem	#S2827
Tat-beclin1 peptide	Sigma-Aldrich	#T1331
bafilomycin A1	Sigma-Aldrich	#B1793
chloroquine	Sigma-Aldrich	#C6628
MLN7243	Chemieteck	#CT-M7243
NMS873	Sigma	#SML1128
4x LDS sample buffer	Thermo Fisher Scientific	#NP0007
RIPA lysis and extraction buffer	Thermo Fisher Scientific	#89900
protease inhibitor cocktail	Roche	#11873580001
Benzonase	Novagen	#70746-4
Protein Assay Dye Reagent Concentrate	Bio-Rad	#5000006
β-mercaptoethanol	Sigma-Aldrich	#M6250
NuPAGE 4–12% bis-tris gradient gels	Thermo Fisher Scientific	#NP0322BOX
MES running buffer	Thermo Fisher Scientific	#NP0002
Immobilon Classico	Merck	#WBLUC0500
SuperSignal West Dura	Thermo Fisher Scientific	#37071

(*Continued on next page*)

Continued

REAGENT or RESOURCE	SOURCE	IDENTIFIER
Paraformaldehyde	Sigma-Aldrich	#47608
Triton X-100	Sigma-Aldrich	#648466
Sucrose	Sigma-Aldrich	#1.07687
Opti-MEM reduced serum medium	Gibco	#31985062
DMEM, high glucose, GlutaMAX	Gibco	#10566016
Fetal bovine albumin	Gibco	#16000044
Penicillin-streptomycin	Gibco	#15140122
TrypLE Express	Gibco	#12604013
PBS	Gibco	#10010023
BSA	Sigma-Aldrich	#9048468
Cellulose acetate membrane	GE Healthcare	#10404131
nitrocellulose membrane	Bio-Rad	#1620150
PVDF membranes	Roche	#3010040001
GFP-Trap	ChromTek	#gtma
RNeasy Mini Kit	Qiagen	#74004
iScript cDNA Synthesis Kit	Biorad	#1708890
PowerUp SYBR Green Master Mix	Thermo Fisher Scientific	#A25742
Syringe filters	Millipore	#SLVG033RS, #SLVM033RS
Mesh filter	Corning	#352235
Quantifoil grids 200 mesh Copper R1/4	Quantifoil Micro Tools	#Q29269
Quantifoil grids 200 mesh Gold R2/1	Quantifoil Micro Tools	#N1-C15nAu20-01
Autogrid support	Thermo Fischer Scientific	
Dynabeads	Invitrogen	#65011
Filter Paper	Whatman	#10311807
Deposited data		
Tomogram 2E	This paper	EMD 18110
Tomogram 3B	This paper	EMD 18114
Tomogram 3E	This paper	EMD 18115
Tomogram S4A	This paper	EMD 18116
Tomogram S4B	This paper	EMD 18117
Tomogram 5B	This paper	EMD 18118
Mass spectrometry datasets	This paper	Pride PXD04426
Raw data for microscopy and immunoblots	This paper	Mendeley data: https://doi.org/10.17632/k66ygh2hy8.1
Experimental models: Cell lines		
HEK293 cells	ATCC	#CRL-1573 (RRID:CVCL_0045)
Experimental models: Organisms/strains		
Neuro2a Htt64Q stable cell line	Wang et al., 1999[59]	RRID:CVCL_D3YS
Neuro2a Htt150Q stable cell line	Wang et al., 1999[59]	RRID:CVCL_D3YT
Oligonucleotides		
On-TARGETplus siRNA MAP1LC3A human	Thermo Fisher Scientific	#s39156
On-TARGETplus siRNA MAP1LC3B human	Thermo Fisher Scientific	#s224996
On-TARGETplus siRNA MAP1LC3C human	Thermo Fisher Scientific	#5s4190
On-TARGETplus siRNA P62 human	Thermo Fisher Scientific	D-001810
Control siRNA	Thermo Fisher Scientific	L-010230
MAP1LC3B CRISPR guide knockout forward: CACCGCGCGCCGTCTCC GGGAGGCA, reverse: aaacTGCCTCCC GGAGACGGCGCGC	This study	Benchling

(*Continued on next page*)

Continued

REAGENT or RESOURCE	SOURCE	IDENTIFIER
MAP1LC3A CRISPR guide knockout forward: CACCGGcttccatgcagtcaggag, reverse: aaacctcctgactgcatggaagCC	This study	Benchling
GABARAP CRISPR guide knockout forward: CACCGAAGATACGCCA CTACCTCAG; reverse: aaacCTG AGGTAGTGGCGTATCTTC	This study	Benchling
GABARAPL2 CRISPR guide knockout forward: CACCGCATGAAGTGGATG TTCAAGG, reverse: aaacCCTTGA ACATCCACTTCATGC	This study	Benchling
ULK1 CRISPR guide knockout forward: CACCGCCACGGTCTCTGTGCCGCCG, reverse: aaacCGGCGGCACAGAGA CCGTGGC	This study	Benchling
Recombinant DNA		
Htt97Q-GFP	Bence et al., 2021[28]	
Htt97Q-myc	Woerner et al., 2016[102]	
Lamp1-RFP	Addgene	RRID:Addgene_45147
mCherry-MAP1LC3B	Addgene	RRID:Addgene_40827
eGFP-MAP1LC3B-RFP	Addgene	RRID:Addgene_84573
Halo-WIPI2B	Addgene	RRID:Addgene 175025
Px330-mCherry	Addgene	RRID:Addgene_98750
Px458-GFP	Addgene	RRID:Addgene #48138
Software and algorithms		
Benchling (RRID:SCR_013955)		https://www.benchling.com/
Fiji/ImageJ 2.15.1 (RRID:SCR_002285)	Schindelin et al., 2012[69]	https://fiji.sc/
GraphPad Prism 9.5.1 (RRID:SCR_002798)	Graphstats Technologies	http://www.graphpad.com/
easyFRAP	Koulouras et al., 2018[103]	https://easyfrap.vmnet.upatras.gr/
MaxQuant v2.5.0.0 (RRID:SCR_014485)	Cox and Mann, 2008[104]	http://www.biochem.mpg.de/5111795/maxquant
LFQ algorithm	Cox et al., 2014[74]	https://adinasarapu.github.io/posts/2018/04/blog-post-lfq/
Perseus 2.0.11 (RRID:SCR_015753)		https://maxquant.net/perseus/
Huygens Essential 21.10.0 (RRID:SCR_014237)	Scientific Volume Imaging	http://svi.nl
3D-Correlation Toolbox 2.2.2	Arnold et al., 2016[62]	https://3dct.semper.space/
SerialEM (RRID:SCR_017293)	Mastronarde et al., 2005[105]	http://bio3d.colorado.edu/SerialEM/
MATLAB R2015b (RRID:SCR_001622)	MathWorks	http://www.mathworks.com/products/matlab/
Tomoman		https://github.com/williamnwan/TOMOMAN
MotionCor2 (RRID:SCR_016499)	Zheng et al., 2017[106]	https://emcore.ucsf.edu/cryoem-software
Exposure filtering	Grant and Grigorieff, 2015[107]	
IMOD 4.11 (RRID:SCR_003297)	Kremer et al., 1996[108]	http://bio3d.colorado.edu/imod
Amira XTracing Module	Rigort et al., 2012[109]	
Amira 2021.2 (RRID:SCR_007353)	Thermo Fisher Scientific	https://www.thermofisher.com/sg/en/home/electron-microscopy/products/software-em-3d-vis/amira-software.html
PyCurv(RRID:SCR_008394)	Salfer et al., 2020[110]	https://github.com/kalemaria/pycurv
TomoSegMemTV 0.85	Martinez-Sanchez et al., 2014[111]	https://sites.google.com/site/3demimageprocessing/tomosegmemtv

(*Continued on next page*)

Continued

REAGENT or RESOURCE	SOURCE	IDENTIFIER
TOM toolbox (RRID:SCR_003220)	Nickell et al., 2005[112]	https://www.biochem.mpg.de/6348566/tom_e
PyTom v0.971	Hrabe et al., 2012[113]	https://pytom.sites.uu.nl/
LisC algorithm	Bäuerlein et al., 2022[114]	https://github.com/FJBauerlein/LisC_Algorithm
Cryo-care v0.2	Buchholz et al., 2019[115]	https://pypi.org/project/cryoCARE/
Topaz	Bepler et al., 2020[116]	https://emgweb.nysbc.org/topaz.html
MaskTomRec	Fernandez et al., 2016[117]	https://sites.google.com/site/3demimageprocessing/masktomrec
AIDA v4.27.039	Elysia Raytest	https://www.elysia-raytest.com/en/cataloglight/c30~aida-image-analysis-software
Zeiss Zen (RRID:SCR_013672)		http://www.zeiss.com/microscopy/en_us/products/microscope-software/zen.html#introduction
LAS X Navigator (RRID: SCR_024857)		https://www.leica-microsystems.com/products/microscope-software/p/leica-las-x-ls/

RESOURCE AVAILABILITY

Lead contact

Further information and requests for resources and reagents should be directed to and will be fulfilled by the lead contact, Dr. Florian Wilfling (florian.wilfling@biophys.mpg.de).

Materials availability

All unique reagents generated in this study are available from the lead contact without restriction or require a completed Materials Transfer Agreement if there is potential for commercial application.

Data and code availability

- The mass spectrometry proteomics raw data have been deposited to the ProteomeXchange Consortium through the PRIDE partner repository with the dataset identifier: PXD044261. Representative tomograms are available in the Electron Microscopy DataBank under the following accession codes: EMD-18110, 18114, 18115, 18116, 18117, 18118. Additional tomographic data can be provided upon reasonable request. Raw data have been deposited to Mendeley datashare: https://doi.org/10.17632/k66ygh2hy8.1. Protocols have been deposited to protocols.io: https://dx.doi.org/10.17504/protocols.io.5qpvokx79l4o/v1, https://dx.doi.org/10.17504/protocols.io.e6nvw1podlmk/v1, https://dx.doi.org/10.17504/protocols.io.dm6gpzexjlzp/v1, https://dx.doi.org/10.17504/protocols.io.261ge5pxyg47/v1, https://dx.doi.org/10.17504/protocols.io.n2bvj3395lk5/v1.
- This paper does not report original code.
- Any additional information required to reanalyze the data reported in this paper is available from the lead contact upon request.

EXPERIMENTAL MODEL AND STUDY PARTICIPANT DETAILS

Cell lines, plasmids, siRNAs, CRISPR-Cas9 knockout, and chemicals

Cells were grown with DMEM + Glutamax (Gibco) with 10% FBS (Gibco) and 100 units/ml Penicillin-Streptomycin (Gibco) in incubator at 37°C with 5% CO2; no unusual Hoechst staining (Cell signaling) observed for mycoplasma contamination. For passages, cells were washed in PBS (Gibco), trypsinized with TrypLE Express (Gibco). Neuro2a containing stable expression of the inducible 64Q- or 150Q-GFP were described before.[16] Early passages in which the 64Q had a higher propensity to form small-dim-amorphous aggregate over the bright fibrillar form (~10:1) was used. For the induction of the transgene expressing polyQ, muristerone A (Abcam) was applied at 1 μM for 2 days. The following chemicals were applied to cell culture: rapamycin (AdipoGen), trehalose dihydrate (Sigma-Aldrich), bafilomycin A1 (Sigma), chloroquine (Sigma), MLN7243 (Chemieteck).

For transient expression, HEK293 were transfected for 48 h using Lipofectamine 3000 (Invitrogen) in Opti-MEM (Gibco) as per manufacturer's protocol, media was refreshed after 24 h. The plasmids expressing GFP and myc tagged Htt97Q exon 1 were described previously.[28,102] Lamp1-RFP, mCherry-MAP1LC3B, eGFP-MAP1LC3B-RFP, and MAP1LC3B-3xflag were obtained from Addgene.

On-TARGETplus SMARTpool siRNA targeting human MAP1LC3A, B, and C, p62 and control were obtained from Thermo Fisher Scientific; 3-day transient knockdown was performed using Lipofectamine. CRISPR-Cas9 knockout in HEK293 of MAP1LC3B, MAP1LC3A, and ULK1 were generated with the px330-mCherry or px458-GFP constructs with the primer guides designed in Benchling. 2-day post transfection, individual positive clones were isolated through fluorescence-activated sorting with a 100 μm nozzle on BD FACSAria III using FACSDiva 6.1.3 software (MPI imaging facility, Martinsried, Germany). The knockdown and knockout efficacies were assayed by immunoblotting for the proteins and/or real-time PCR for the transcripts.

METHOD DETAILS

Immunoblotting and filter trap slot blots

The following antibodies were used for immunoblotting: mouse anti-GFP (Santa Cruz), rabbit anti-GFP (Roche), anti-MAP1LC3B (Sigma, Santa Cruz), anti-beta-actin (Abcepta), Anti-Tubulin (Sigma), Goat anti-rabbit HRP (Sigma), Goat anti-mouse HRP (Sigma).

Cells from a well of 12-well plate were lysed on ice in 80 μL RIPA buffer (Thermo) supplemented with protease inhibitor cocktail (Roche) and Benzonase (Novagen) with intermittent vortexing. Protein concentration in total cell lysates was determined using Protein Assay Dye Reagent Concentrate (Bio-Rad), normalized before denaturing in 4x LDS sample buffer (Thermo) containing 2.5% β-mercaptoethanol (Sigma) and boiling at 95°C for 5 min. Proteins were separated on NuPAGE 4–12% bis-tris gels (Thermo) with MES running buffer (Thermo). Afterward, proteins were transferred to PVDF membranes (Roche) in tris-glycine buffer using semi-dry transfer. Membranes were washed in TBS-T and blocked in 5% low-fat dry milk dissolved in TBS-T for 1 h at room temperature. Blots were incubated with primary antibodies (1:500-1:1000) overnight at 4°C, washed 3 times with TBS-T and probed with HRP-conjugated secondary antibodies (1:10000) for 1–2 h at room temperature. Chemiluminescence was developed using HRP substrate Immobilon Classico (Merck) or SuperSignal West Dura (Thermo), detected on an ImageQuant800 (Amersham) imager with control software v1.2.0. Intensity of protein bands was quantified using AIDA image software v4.27.039 (Elysia Raytest).

Filter-trap assay for the detection of aggregated HttQ64-GFP was performed as before.[34] Lysates were prepared as described in immunoblotting. 10 or 20μg total protein was diluted in 100μL or 200μL RIPA. Cellulose acetate membrane (0.2μm pore, GE Healthcare) was equilibrated in 0.1% SDS/H_2O and fixed to the filter trap device (PR648 Slot Blot Blotting Manifold, Hoefer). Samples were loaded under vacuum. Slots were then washed with 200μL 0.1% SDS/H_2O 3 times followed by standard immunoblotting.

For dot blot detection of total cellular lysates, cells were lysed in lysis buffer as above followed by denaturation in sample buffer, and were loaded onto nitrocellulose membrane (Bio-Rad) in a dot blot apparatus (GE Healthcare). Thereafter, the membrane was dried for standard immunoblotting.

Transcript level quantification

Total RNA was isolated using the RNeasy Mini Kit (Qiagen) and reverse transcribed using iScript cDNA Synthesis Kit (Biorad) primed with oligo-dT according to manufacturers' instructions. Quantitative real-time PCR was performed with PowerUp SYBR Green Master Mix (Applied Biosystems) with a StepOnePlus Real-Time PCR System (Applied Biosystems). CT values were measured and fold changes and were calculated by the ΔΔC(T) method using the RPS27 gene as the reference. Expression level in the knockouts is displayed with transcript level from the control cell normalized to 100%. The following primers were used for real-time PCR quantification: MAP1LC3A: forward 5′-CCCAAACCGCAGACACATCCCC-3′ and reverse 5′-GCTGGTCGCGGATCTGCTGTAC-3′, MAP1LC3B: forward 5′-CAGGGGTTCGAGACCAGCCTGA-3′ and reverse 5′-TGCCGTCAGGTAGGAAGTGGGG-3′, ULK1: forward 5′-TTTGGAGGTCGCCGTCAAGTGC-3′ and reverse 5′-TGGAAGTCGTACAGGGCCACGA-3', GABARAP: forward 5'-CCCAC CAGTGCCACAATGGGTC-3' and reverse 5'-CAGGGGCAGCAGCTTCACAGAC-3', GABARAPL2: forward 5'-CACTCGCTGGAACA CAGATG-3' and reverse 5'-TCCACATGAACTGAGCCACA-3'.

Confocal fluorescence light microscope image acquisition and analysis

The following antibodies were used for immunostaining: anti-myc (Millipore); anti-MAP1LC3B (Novusbio); anti-Ubiquitin (Santa Cruz); anti-p62 (Enzo); anti-polyQ (Sigma), goat anti-rabbit Alexa Fluor 555 (Thermo), goat anti-mouse CF350 (Sigma), and Janelia Fluor HaloTag ligand 549 (Promega).

Cells were seeded onto glass coverslips in 6-well cell culture plates. Cells were washed with PBS and fixed in 4% paraformaldehyde (Sigma) for 10 min, permeabilized with 0.1% Triton X-100 (Sigma) for 5 min, and blocked in 5% milk in PBS at room temperature for 1 h. Primary antibodies were applied at a dilution of 1:50-1:100 in block overnight at 4°C, then washed in PBS (2 × 5 min) and incubated with secondary antibodies at a dilution of 1:1000 in dark at room temperature for 1 h. Coverslips were washed with PBS (3 × 5 min), mounted onto glass slides with Fluoromount (Sigma).

For staining with ER-Tracker Red or LysoTracker red DND-99 (Invitrogen) or Janelia Fluor HalotTag 549, the dyes were added to the culture prior to fixation or vitrification according to the manufacturer's protocol. 30 min prior to vitrification or live confocal light

microscope imaging, cells were also stained with Annexin V-pacific blue (Invitrogen) or iFlour 555 (Abcam) according to the manufacturer's protocol to quantify and exclude apoptotic cells from further analysis, respectively.

Fluorescence microscopy data were acquired at the MPI imaging facility, on a confocal laser scanning microscope (Zeiss LSM 780, Jena, Germany) with a PLAN/APO 63× oil objective and the Zeiss Zen software. Images acquired with the Airyscan 2 detector was performed on the Zeiss LSM 980 microscope. For fixed slides, images for quantifications of control and the treatments were taken with the same exposure setting at around the aggregate equator, data analysis was performed in Fiji.[69] Representative datapoints from reproducible experiments shown. The measurements of the aggregate cross-sectional areas were carried out with the central zone thresholded to >8000 for GFP intensity (threshold tool), and the peripheral region set to 800–8000 for the intensity threshold. Fluorescence analyses of LysoTracker and MAP1LC3B staining were performed similarly using threshold tool with signal intensity >800 across samples, the area within ~1.5 μm around the central zone was quantified quantified. Data analyses were performed in GraphPad Prism 9 (Graphstats Technologies), *p* values generated from two-tailed student's paired t test.

Confocal live imaging was acquired in Zeiss LSM 980 Airyscan 2 with PLAN/APO 63× oil objective, with cells in 5% CO_2 and 37°C. Z stacks of the aggregates were generated by scanning at 0.5 μm interval for a 7 μm span. FRAP assay was carried out for the tracking with single frames imaged at 20 s intervals for ~400s. FRAP analysis was performed with double normalization using the easyFRAP software tool.[103]

Isolation of mCherry-LC3B and 97Q-GFP vesicles and LC-MS/MS

The isolation of mCherry-LC3B and Htt97Q-GFP vesicles was carried out as following[75] with minor modifications. Co-transfected HEK293 or Neuro2a were grown in 6-well plates for 48 h with or without treh/rapa and torin1. Autophagy degradation of the vesicle content was inhibited by bafilomycin A1 (100nM) or chloroquine (100μM) for 5 h prior to harvest. Cells were harvested and homogenized with 22-gauge needle in 1.5mL cold isotonic buffer (0.25M sucrose, 1mM EDTA, 20mM HEPES pH 7.4) with protease inhibitor. Lysates were centrifuged at 800 g at 4°C for 10 min to pellet the nuclei. The supernatant was then centrifuged at 10,000g for 20 min at 4°C, the pellet was collected and washed in PBS to remove free mCherry-LC3B. The pellet was then resuspended in PBS and filtered (Corning) to remove clumps prior to vitrification, analyses by confocal microscope or by flow cytometry sorting (Imaging facility).

Flow cytometry sorting was performed with a 70 μm nozzle on a BD FACSAria III with standard calibrations by fluorescence beads. A negative control without the tagged proteins was included as background control. Vesicles < ~1μm diameter were sorted and collected in PBS, and were applied to dot blots or processed for LC-MS/MS (Biochemistry core facility) in triplicates.

For LC-MS/MS, proteins were reduced and alkylated in SDC buffer (1% Sodium deoxycholate, 40 mM 2-Cloroacetamide (Sigma), 10 mM TCEP (Thermo) in 100 mM Tris pH 8.0) for 20 min at 37°C. The samples were then diluted with MS grade water (VWR) and digested overnight at 37°C with 1 μg Lys-C (Labchem-wako) and 2μg trypsin (Promega), followed by acidification with Trifluoroacetic acid (Merck) to 1% (pH < 2). Next, the samples were purified via Sep-Pak Vac 1cc (50mg) tC18 Cartridges (Waters GmbH) with 0.1M acetic acid (Roth) wash and eluted with 80% Acetonitrile and 20mM acetic acid (Roth), and vacuum dried for resuspension in Buffer A (0.1% (v/v) Formic acid (Roth)). Peptides were then loaded onto a 30-cm column (packed with ReproSil-Pur C18-AQ 1.9-micron beads, Dr. Maisch GmbH) via the Thermo Easy-nLC 1200 autosampler (Thermo) at 60°C. Using the nano-electrospray interface, peptides were sprayed onto the Orbitrap MS Q Exactive HF (Thermo) in buffer A at 250 nL/min, and buffer B (80% Acetonitril, 0.1% Formic acid) was ramped to 30% in 60 min, 60% in 15 min, 95% in 5 min, and finally maintained at 95% for 5 min. MS was operated in a data-dependent mode with survey scans 300–1650 m/z (resolution of 60000 at m/z = 200), and up to 10 top precursors were selected and fragmented using higher energy collisional dissociation (HCD with a normalized collision energy value at 28). The MS2 spectra were recorded at a resolution of 30000 (at m/z = 200). AGC target for MS and MS2 scans were set to 3E6 and 1E5 respectively within a maximum injection time of 100 and 60 ms for MS and MS2 scans respectively. Dynamic exclusion was set to 30ms.

Raw MS data were processed using the MaxQuant platform[104] with standard settings, and searched against the reviewed Human or Mouse Uniprot databases, as well as mCherry-LC3B and polyQ-GFP sequences, allowing precursor mass deviation of 4.5 ppm and fragment mass deviation of 20 ppm. MaxQuant by default enables individual peptide mass tolerances. Cys carbamidomethylation was set as static, and Ub, Met oxidation and N-terminal acetylation as variable modifications. Protein abundances within a sample were calculated using iBAQ intensities[118] and were quantified over the samples using the LFQ algorithm[74] for analysis with the Perseus software (https://maxquant.net/perseus/).

Anti-GFP pull-down with syringe filter partition

Htt64Q-GFP induced in Neuro2a for two days in a 15cm dish, wash with PBS, and were lysed in cold isotonic buffer (0.25M sucrose, 1mM EDTA, 20mM HEPES pH 7.4) with protease inhibitor using gauge 22-needle. Nuclei were pelleted at 800g for 10 min at 4°C, supernatant was then centrifuged at 16000g for 10 min at 4°C to pellet aggregates and the associated proteins. The pellet was washed once in PBS to remove soluble Htt64Q-GFP and was then dissolved in PBS, and passed through pre-equilibrated syringe filters with 0.2um or 0.4um pore sizes (Millipore). The filter blocked fractions were collected and pelleted again at 16,000g for 10 min at 4°C. The fractions were then incubated with magnetic GFP-Trap (ChromTek) for 6 h at 4°C in binding buffer (140 mM NaCl, 25 mM Tris pH 7.6–8.0, 0.5% NP40, 1 mM EDTA) and 2% BSA (Sigma). Lysates from cells without muristerone A induction was used as negative control in pull down. After 5 washes with the binding buffer, the bound fraction was eluted and denaturation in sample buffer for dot blot analysis.

Sample vitrification for cryo-ET

Cells were seeded on holey carbon-coated 200 mesh gold EM grids (Quantifoil Micro Tools, Jena, Germany) in 35 mm cell culture dishes. Prior to vitrification, cells were applied with DMEM containing 10% glycerol as a cryo-protectant and Dynabeads (Invitrogen) at 1:40 dilution for 3D CLEM workflow, then immediately mounted on Vitrobot Mark IV (Thermo), blotted from the back side using FEI Vitrobot Perforated Filter Paper (Whatman) with force 10 for 15 s at room temperature, and plunged into a 2:1 ethane:propane mixture cooled down to liquid nitrogen temperature. Plunge-frozen grids were then clipped into Autogrid support frames modified with a cut-out (Thermo), stored in liquid nitrogen, and maintained at $\leq -170^{\circ}$C for all steps.

For the vitrification of isolated vesicles, 4 μL of the sample was applied to glow discharged holey carbon-coated 200 mesh copper EM grids (Quantifoil Micro Tools), vitrified as above at 4°C and 100% humidity.

Correlated light-electron microscopy (CLEM) and cryo-focused ion beam (FIB) milling

Vitrified sample on autogrids were loaded onto a cryo-confocal LM set up (Leica SP8) equipped with a 50X/0.9 NA objective (Leica Objective), metal halide light source (EL6000), air-cooled detector (DFC900GT), a cryo-stage (-195°C), and two HyD detectors. The sample was kept in liquid nitrogen vapor, following a similar workflow as described.[64] Cryo-confocal z stacks (step size 500 nm, x-y pixel size 85 nm) were taken with pin hole = 1, and a 9 μm depth with the LAS X Navigator software, using 488 and 552 nm laser excitation for GFP and RFP tagged proteins, respectively, also picking up signals from the auto-fluorescent Dynabeads. To improve signal clarity, image stacks were de-convoluted and restored with Huygens Essential software (Scientific Volume Imaging) to remove noise. The stack was then imported into the 3Dcorrelation software[62] and re-sliced into cubic voxels.

For preparing the lamella (150–250 nm), autogrids were mounted into a Quanta dual-beam 3D FIB/scanning electron microscope (Thermo) equipped with a transfer shuttle system (PP3000T, Quorum) at $< -180^{\circ}$C throughout milling. To protect the milling front of the lamella, gaseous organometallic platinum was sprayed onto the sample on the cryo-stage using a gas injection system. To target the cell for milling, the grid square was correlated with the cryo-confocal fluorescence z stack using the 3Dcorrelation software. The target was imaged and correlated iteratively with the z stack throughout milling for accuracy. The 12–15 μm wide lamellas were generated using a Gallium FIB at 30 kV with a 20° stage angle in three consecutive steps. The more distant region (>2 μm) above and below the target was rough milled with a higher current of 500 pA, followed by fine milling to a ~800 nm lamella using a current of 100 pA. A final polishing of the lamella to thickness of 150–250 nm was carried out with a 30–50 pA current. Lamella final thickness was estimated with SEM at 3 keV, for a lack of overcharging.

Cryo-ET data acquisition, tomogram reconstruction, and analysis

Lamellas were imaged in a FEI G2 Polara or Titan Krios cryo-TEM equipped with a field emission gun operating at 300 kV, a post-column energy filter (Gatan, Pleasanton, CA, USA) operating at zero-loss, and a 4k x 4k K2 Summit direct electron detector (Gatan). The energy filter was used to increase image contrast with a slit width of 20 eV. Low-magnification were taken at 5600x (object pixel size 2.18 nm) to generate lamella overviews. The lamella overview acquired in the cryo-TEM may have a 180° rotation with respect to the FIB/SEM image due to the orientation of sample loading for the cryo-TEM. High-magnification (18,000x, 27,500x, 34,000x, 42,000x) with a pixel size of 0.65, 0.42, 0.34, 0.32 nm respectively) tilt series were recorded at sites of interest using the SerialEM software,[105] operating in low dose mode with tracking and focus enabled. Tilt series were taken with a 2° tilt increment with an angular range from ~-60° to 60°. The K2 camera operating in dose fractionation counting mode, recorded frames every 0.2 s for ~2 electrons/A^2 per tilt angle. For the tilt series, the cumulative dose was in the range of 90–120 electrons/Å^2. Targeted defocus of -9 μm (Polara) or -5 μm (Krios) were applied to boost contrast. The low magnification views (5600×) of the lamella provided enough detail to locate the aggregates and surrounding structures for tomogram acquisitions.

For tilt series acquisition of the isolated vesicles, Htt97Q-GFP and LC3B-RFP positive puncta were first located on the vitrified grid using the Leica cryo-confocal LM. Sample features including holes and cracks were used as landmarks for target identification.

K2 camera raw frames were preprocessed using in-house Matlab[112] wrapper scripts (Tomoman: https://github.com/williamnwan/TOMOMAN). The relative shifts of the image between camera frames due to stage drift and beam-induced motion were corrected by MotionCor2,[106] followed by exposure filtering.[107] The tilt series were then aligned using patch tracking, binned by 4, and reconstructed by weighted back projection in IMOD.[108] FIB-related imperfections of the lamella were removed for image display, using the LisC filter algorithm.[114] Tomogram contrast was improved using Topaz[116] or cryo-care.[115] Ice contamination were removed from the tomogram using the MaskTomRec software.[117] The overlays of fluorescence z stack, SEM, and TEM images were generated using the Transform/Landmark correspondence plugin (Fiji).

Tomogram segmentation was performed in Amira (Thermo). Membranes were automatically detected by TomoSegMemTV using tensor voting,[111] followed by manual refinement in Amira. polyQ fibrils were detected using the XTracing module.[109] In brief, tomograms were denoised by a non-local means filter, and the fibril containing regions were searched for a cylindrical template of 8 nm (diameter) and 42 nm (length). The resulting cross-correlation fields were adjusted to a range of 0.68–0.8 for optimized detection. The amorphous aggregate density was approximated by fluorescence correlation, the corresponding region was segmented by the magic wand tool in Amira. The cytosolic ribosomes were detected by PyTom template matching,[113] using a low pass filtered (60 Å) ribosome template (EMDB: 5592). Based on the segmented membrane, the intermembrane distance and the thickness of the phagophore double layers were calculated with the PyCurv software,[110] using aligned and exposure filtered tomograms (Titan Krios bin 4 pixel size at 12.76 Å).

From aligned and exposure filtered tomogram dataset (Polara bin 4 pixel size at 26.38 Å) without additional contrast enhancement, the diameters and relative intensities of the interior volume of the phagophores and autophagosomes, as well as the downstream vesicles (autolysosomes and lysosomes) were quantified in Fiji. Diameters (nm) were taken as the longest distance of the inner bilamellar membrane of phagophores and autophagosomes, or the longest distance between the uni-lamellar downstream vesicles. Relative intensity of the interior volume was calculated as the average intensity of the volume inside the phagophores and autophagosomes, or the downstream vesicles, normalized to the average intensity of the entire tomogram, excluding regions with ice crystals and broken edges.

QUANTIFICATION AND STATISTICAL ANALYSIS

To present quantitative data, Microsoft Excel v.16.0.10406.20006 and GraphPad Prism v.9.5.1 were utilized and figures are structured in Adobe Illustrator 2023. Unless otherwise stated in the figure legends, *p*-values for quantification of fluorescence microscopy and TEM data were generated by two-tailed Student's t test. Western blot data displayed were representative experiments, and the number of independent experiments from biological replicates conducted is indicated in the legend.